P- and *S*-velocity anomalies in the upper mantle beneath Europe from tomographic inversion of ISC data

I. Koulakov,[1,2] M. K. Kaban,[2,3] M. Tesauro[2,4] and S. Cloetingh[4]

[1]*IPGG SB RAS, Novosibirsk, Russia. E-mail: KoulakovIY@ipgg.nsc.ru*
[2]*GeoForschungsZentrum, Potsdam, Germany*
[3]*IPE RAS, Moscow, Russia*
[4]*Vrije Universiteit, Amsterdam, the Netherlands*

GJI Seismology

SUMMARY

We present a new tomographic model for *P*- and *S*-velocity anomalies beneath Europe (30°N–55°N, 5°W–40°E), extending in depth up to 700 km and constrained by inversion of data from the International Seismological Center (ISC) catalogue. The algorithm uses the traveltimes from events located in the study area recorded by all available worldwide stations, as well as times from teleseismic events recorded by European stations. The events from the ISC catalogue have been relocated and combined into composite events. All the traveltimes were corrected for crustal structure using the reference model EuCRUST-07. The resulting velocity anomalies show similar large-scale patterns as observed in previous studies, but have a higher resolution, which allows detection of some features in more detail. For example, it is now possible to assess the depth extension of the small slow velocity body beneath the Eifel region and Eger graben. The *P* and the *S* model show a good consistency in the uppermost 200 km below most of the European area and in some parts even in the deeper layers (e.g. beneath the Apennines and the Hellenic arc). The new model provides clear images of some principal features, which were previously detected in a limited number of studies, while the comparison between *P*- and *S*-velocity anomalies provides novel constraints to address on their nature (e.g. the gap in the Adriatic plate subducted below the central-southern Apennines). In this paper, we pay special attention to testing the reliability of the results. The random noise effect is evaluated using a test with independent inversion of two data subsets (with odd/even events). The spatial resolution is estimated using different checkerboard tests. Furthermore, we present a synthetic model with realistic patterns, which reproduces after performing forward and inverse modelling the same shape and amplitudes of the anomalies as in the case of the real data inversion. In this case, the parameters of the model can be used to assess the amplitudes of *P* and *S* anomalies that is critical for evaluation of other petrophysical parameters (temperature, density, composition, etc.) in the upper mantle.

Key words: Mantle processes; Seismic tomography; Subduction zone processes; Crustal structure; Europe.

1 INTRODUCTION

The European region is an optimal natural laboratory for probing and calibrating seismic algorithms to investigate the deep Earth interior. Hundreds of seismic stations, operating permanently since a long time, fairly dense cover most of Europe. They provide high-quality information on traveltimes from local, regional and teleseismic events. Furthermore, in Central and Southern Europe relatively high-seismic activity is present both in terms of frequency and magnitude. The events located along the African-Eurasian plate boundary (e.g. in the Mediterranean) and within Central Europe (e.g. along the European Cenozoic Rift System) are mostly recorded by dozens

of regional stations and often by worldwide stations. The high level of tectonic activity in Central and Southern Europe (see the main tectonic units in Fig. 1) has a strong connection with lithosphere and deep mantle processes. As a clear example, the ongoing collision of African and Eurasian plates, which produces compressional stresses along the plate boundary, results in subduction of the cold African lithosphere into the European mantle. On the other hand, some areas of Central and Western Europe (e.g. the Rhine Graben) are characterized by extensional tectonics and stresses (e.g. Olaiz *et al.* 2009), which are probably related to Cenozoic upper-mantle plume activity (e.g. Ziegler 1992). These tectonic processes are related to strong seismic heterogeneities in the mantle, which can be detected by
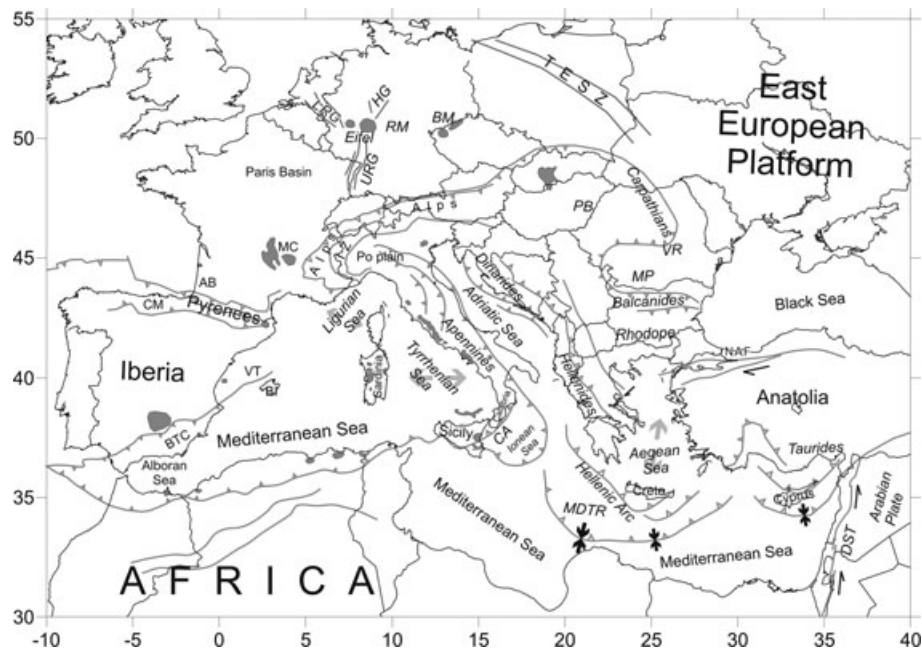
Figure 1. Main geographic and tectonic elements in the study area modified after Faccenna *et al.* (2003). Grey spots indicate the main Cenozoic volcanic fields (Ziegler & Dezes 2006). Abbreviations: AB, Aquitaine Basin; BI, Balearic Islands; BM, Bohemian Massif; BTC, Betic Cordillera; CA, Calabrian Arc; CM, Cantabrian Mountains; DST, Dead Sea Transform; HG, Hessian Graben; IZ, Ivrea Zone; LRG, Lower Rhine Graben; MP, Moesian Platform; MC, Massif Central; MDTR, Mediterranean Ridge; NAP, North Anatolian Fault; PB, Pannonian Basin; PRM, Rhenish Massif; TESZ, Trans European Suture Zone; URG, Upper Rhine Graben; VR, Vrancea; VT, Valencia Trough; WC, West Carpathians.

seismic tomography methods. Furthermore, a large amount of different geophysical studies in Europe allows a comparison of different approaches and obtained results. In particular, the velocity structure of the lithosphere obtained in regional tomography studies can be compared with reflection/refraction seismic sections and receiver functions determinations, which are rather dense in Europe. This provides a robust basis for verification of the algorithms employed in seismic tomography. Ziegler 2006

Tomographic investigations of the European deep structure started in the early eighties and were based mostly on body waves (Romanowicz 1980; Hovland *et al.* 1981; Granet & Tranpert 1989). In the nineties, more detailed images of *P* velocity anomalies have been obtained for some regions like the Hellenic arc (Spakman 1991), the Iberian Peninsula (Blanco & Spakman 1993), the western (Gobarenko *et al.* 1990) and the entire Mediterranean (Spakman *et al.* 1993). The results of these first studies are already in reasonably good agreement with the geodynamic concept of the lithosphere evolution in the Mediterranean region (de Jonge *et al.* 1994). Later on, the more detailed V_p structure beneath Europe, obtained by Bijwaard *et al.* (1998) within a framework of the global tomography model, was successively employed in geodynamic reconstructions (e.g. Wortel & Spakman 2000). Other regional tomographic models in Europe demonstrate generally the same patterns of *P*-wave anomalies, although the mid- and small-scale features are still rather different (e.g. Piromallo & Morelli 2003). In the regional study of Hearn (1999) the first anisotropic V_p structure has been obtained for the uppermost mantle beneath Italy and surrounding areas based on traveltimes of *Pn* rays.

The constructed *S*-wave models are less consistent than the *P* wave ones. In the last decades several studies were performed to investigate V_s distribution in the European upper mantle (Berry & Knopoff 1967; Panza *et al.* 1980; Calcagnile & Panza 1981; Calcagnile *et al.* 1982; Marillier & Mueller 1985). Most of the regional *S*-velocity models are based on surface wave tomography, which has lower horizontal resolution than the body wave studies used to constrain the *P*-velocity models. Some attempts were made to increase the horizontal resolution. For instance, Snieder (1988) analysed high-frequency surface waves but at the expense of a limited depth resolution. Zielhuis & Nolet (1994) have tried to increase both the horizontal and vertical resolution by applying the Partitioned Waveform Inversion (PWI) method (Nolet 1990) and obtained the *S*-wave model with more details in the upper mantle. A continuous improvement of the V_s models allowed their employment jointly with V_p models in geophysical applications. An example is given by the estimation of the temperature distribution in the European upper mantle (Goes *et al.* 2000) obtained by inversion of the *P*- (Bijwaard *et al.* 1998) and *S*-velocity (Marquering & Snieder 1996) models. Therefore, it appears that the existing V_p (e.g. Spakman 1993; Piromalllo & Morelli 2003) and V_s models (e.g. Martinez *et al.* 2000; Pasyanos *et al.* 2001; Marone *et al.* 2004; Pasyanos 2005) show similar large-scale velocity patterns in the European mantle (e.g. high-velocity traces of subduction beneath the Alpine and Hellenic arcs), whereas these models can be remarkably different in regional details. One of the reasons for such discrepancies could be a trade off with crustal heterogeneities propagated in the mantle velocity model.

Differentiation between crustal and upper-mantle structure is one of the main problems of seismic tomography. For example, the effect of crustal thickness variations on traveltimes is equivalent to very strong velocity anomalies in the adjacent layers. It has been demonstrated that the employment of a crustal model in global tomography allows to determine a more reliable velocity distribution in the upper mantle (e.g. Ekstrom & Dziewonski 1998). In Europe only some of the local traveltime tomography models are obtained including an *a priori* crustal model (e.g. Waldhauser *et al.* 2002; Lippitsch *et al.* 2003; Sandoval *et al.* 2003; Martin *et al.* 2006).

These studies already demonstrate the importance of careful *a priori* correction of the teleseismic traveltime residuals for 3-D crustal structure. In some cases, neglecting an *a priori* crustal correction in the traveltime tomography might even lead to an error in the anomaly sign. For instance, Piromallo & Morelli (2003) have found a strong negative anomaly in the uppermost mantle under the South-eastern Carpathians and Focşani foredeep (up to −7 per cent). By contrast, the seismic tomography inversion of Martin *et al.* (2006) corrected for the crustal effect leads to high velocities (+3.5 per cent) in the upper mantle in this area. Waldhauser *et al.* (2002) have demonstrated that even non-linear inversion of the synthetic residuals without correcting for the 3-D crustal structure erroneously maps the crustal anomalies into the upper mantle.

In this study, we present a new tomographic model of *P*- and *S*-velocity anomalies in the European mantle based on inversion of body wave traveltimes, which are corrected for the crustal structure obtained from independent data sources. The new model is produced using the algorithm of Koulakov & Sobolev (2006) and the reference model of the European crust EuCRUST-07 (Tesauro *et al.* 2008). The algorithm has already been utilized in investigations of the upper-mantle structure beneath the entire Alpine-Himalayan orogenic belt (Koulakov *et al.* 2002), Southern Siberia and Mongolia (Koulakov 1998, 2008), Pamir-Hindukush region (Koulakov & Sobolev 2006) and Iran (Alinaghi *et al.* 2007).

The constructed model covers the area within 30°N–55°N, 5°W–40°E and extends to a depth of about 700 km. In this work, we pay special attention to testing. For this aim the results were verified using the test with odd/even events, which reveals the effect of a random noise, and different synthetic reconstructions. As already mentioned, despite general consistency of the existing tomography models, they differ in details. This is also true for reproduced amplitudes of the velocity anomalies. These amplitudes depend on many factors including inversion parameters. We have constructed a synthetic model with a realistic configuration of anomalies, which can be used to estimate the amplitudes of the real velocity anomalies. These amplitudes are important for a correct determination of petrophysical parameters (e.g. temperature, density andcomposition) in the upper mantle. The obtained results are compared with those of previous studies.

2 DATA AND ALGORITHM

2.1 Traveltimes

The initial data used in this study include traveltimes of *P* and *S* body waves reported by the International Seismological Center (ISC 2001). The undoubted advantage of the ISC data, compared to local networks, is their large time span and global coverage. On the other hand, the locations of the sources, provided by the ISC, are not precise and need to be revised. The errors are mainly related to oversimplified standard techniques used for source location and to the outdated 1-D velocity JB model (Jeffreys & Bullen 1940).

All events in the time period from 1964 to 2001 were localized using the algorithm described in Koulakov & Sobolev (2006). This algorithm takes into account the surface relief, ellipticity of the Earth and Moho depth (model CRUST2.0, Bassin *et al.* 2000). Furthermore, the depth phases (pP and sS) were used to improve depth location of the sources. In this algorithm special attention was paid to the problem of rejecting outliers, which take a considerable part in ISC catalogue (∼25–30 per cent). We use only the events with the azimuthal GAP of less than 180°. The residuals higher than 4 and 6 s for *P* and *S* data, respectively, have been rejected. The minimal number of the recorded *P* and *S* phases considered at all available epicentral distances for the events is 30.

To reduce the disproportion of the data distribution, all the earthquakes in the entire catalogue have been combined into composite events. A similar approach was used by Bijwaard *et al.* (1998) to compute the global tomographic model. The Earth was subdivided in 3-D cells. Along latitude the cells size is equal to 0.3°. The longitudinal step is varied along the latitude to provide an isometric shape of the cells (∼30 km). The depth step depends on a depth (from 10 km in the crust to 50 km in the mantle). All the events located in one cell were replaced with one composite event. If several events in one cell were recorded by one station, we performed a correlation analysis between these rays. If the difference between the individual and the average residuals for all rays from one segment was larger than 1 s, the corresponding ray was rejected as erroneous. The remaining rays were replaced with one composite ray and the residuals were averaged. The combination of the events and correlation analysis of the residuals leads to a significant improvement of the data quality.

The amount of *S* picks is significantly lower than that of *P* picks. For the teleseismic rays recorded by the European stations the number of *S* picks is about 10 times smaller. For some areas (e.g. in France) the teleseismic *S* picks are almost not presented in the ISC catalogue. Therefore, *S*-velocity structure beneath such areas cannot be investigated using these data. Furthermore, the accuracy of the *S* picks is quite low, which was also indicated in many previous data analysis studies (e.g. Engdahl *et al.* 1998). Thus, the *S*-velocity results should be considered with prudence, especially for mantle depths.

In this study, the inversion was performed separately in several circular windows, which cover the entire study area and overlap each other (Fig. 2). After computing the results in all areas, they are combined in one model for the entire study area. In total we used 12 windows with a radius of 7°. As was shown in Koulakov & Sobolev (2006), this size provides an optimal ray configuration for investigating the upper mantle down to 700 km depth. For the inversion we used two types of data. One data group includes traveltimes from the events located inside the current circular window and recorded by the stations (Fig. 2) at any available epicentral distances. Any event was taken into consideration if the number of phases exceeds 50. The other data group includes the residuals corresponding to the events located outside the current window and recorded by the stations located inside (Fig. 2). In this study, the minimum number of stations inside the window, which recorded an outside event, was fixed at 60. The number of rays in separate areas varies from ∼40 000 to 720 000, depending on the window. For the entire area we used more than 2 millions rays.

2.2 Algorithm

The tomographic inversion is based on a linearized approach. The calculations are performed based on the rays constructed in the 1-D spherical model AK 135 (Kennett *at al.* 1995), using only one iteration. In principle, it would be technically possible to adapt non-linear iterative approaches to this case (for example, LOTOS algorithm developed by Koulakov *et al.* 2007; Koulakov 2009), but this would strongly increase the calculation time. According to our estimates, performing one run for the entire area based on 3-D tracing of several millions of rays would take at least one week or longer computing time.

The expected amplitude of the velocity anomalies in the mantle does not exceed 4–5 per cent. For such amplitudes, the non-linear
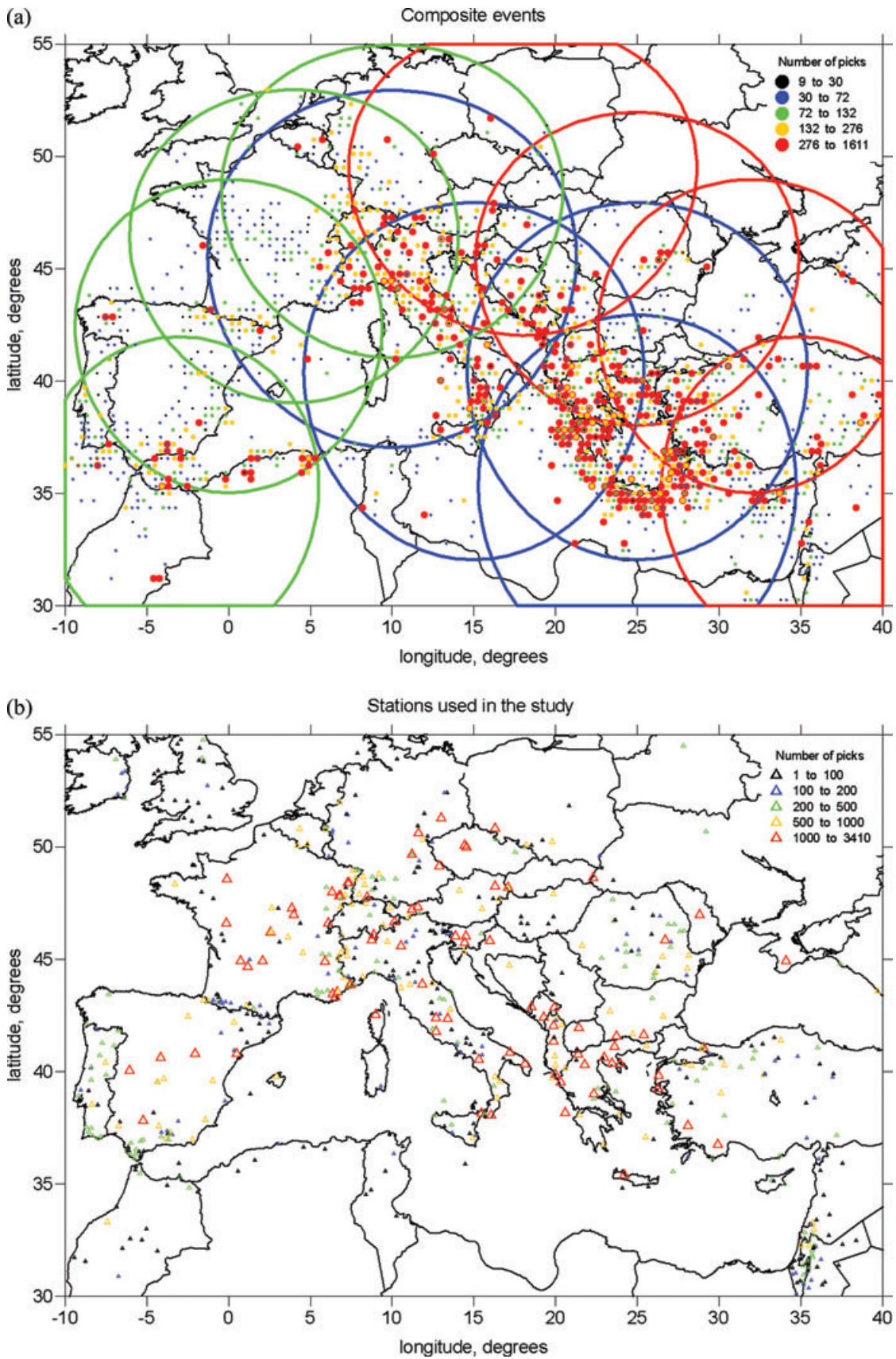
Figure 2. (a) Distribution of composite events used in this study. Colours of dots represent number of *P* and *S* picks for each event. The circles limit the areas in which separate inversions were performed. (b) Distribution of stations used in this study. Colour and size of triangles represent the number of picks recorded by each station from the composite events used in this study.

effects should be small and can be neglected (e.g. Nolet 1987). Even in areas with very strong heterogeneities (e.g. in Central Java with anomalies of 30 per cent, Koulakov *et al.* 2007) performing non-linear iterative approach does not much affect the shapes of the main patterns. In these cases an underdamped solution in one iteration (linear approach) may appear to be identical to an overdamped solution after several iterations. Therefore, it is more logic to perform additional tests and calculations for several real and synthetic models. It is obvious that in the case of non-linear inversion the number of these tests would be significantly limited, which is more severe than the errors related to the non-linear effects. Having the opportunity to perform many trials in a relative short time is important for the determination of optimal free parameters. Unfortunately, there are no routine tools for their fast estimations. Many tomographers use trade-off curves to find the best damping. However, the study of Koulakov (2009) has shown that the damping value computed in this way is not appropriate. Therefore, the performance of synthetic modelling gives the best chance to estimate the free parameters. Successively, the parameters can be adjusted in order to improve the quality of the synthetic anomalies. The values of the parameters are optimized by increasing the number of the tests performed. The synthetic tests are described in more details in Sections 3.4 and 3.5.

Traveltimes and ray paths in the spherical 1-D model were computed using the algorithm presented in Nolet (1981). The average Moho depth in the reference model was defined at 40 km. The non-spherical component includes the corrections for the station elevation and crustal effects. The crustal corrections were computed using EuCRUST-07, a new reference model of the European crust (Tesauro *et al.* 2008). This model includes information about Moho (H_{moho}) and upper/lower crust (H_{ULCD}) depth, as well as upper and lower crust velocities (V_{up} and V_{low}, respectively).

The crustal time correction (Fig. 3) consists of two terms: crustal velocity correction, dt_{vel}, and Moho depth correction, dt_{moho}.

$$dt_{data} = dt_{obs} - dt_{moho} - dt_{vel}, \tag{1}$$

where dt_{obs} is the observed residual computed after relocation. The term dt_{vel} is computed by integrating along a ray segment passing in the crust

$$dt_{vel} = -\int_{\gamma_{crust}} \frac{V_{crust} - V_{ref}}{V_{ref}^2} ds, \tag{2}$$

where V_{ref} is the velocity according to the 1-D reference model (AK135, Kennett *et al.* 1995); V_{crust} is the velocity according to the model EuCRUST-07 (Figs 4a and b). It depends on the depth of the current point, z, and is equal to

$$V_{crust} = \begin{cases} V_{up} & \text{if } z > H_{ULCD} \\ V_{low} & \text{if } z < H_{ULCD} \end{cases}. \tag{3}$$

S velocities are computed from the values of V_p velocities given in EuCRUST-07 using the V_p/V_s ratio according to the 1-D reference model (AK135, Kennett 1995).

The correction dt_{moho} is computed as

$$dt_{moho} = (H_{moho} - H_{ref})\left(\sqrt{1/V_1^2 - p_x^2} - \sqrt{1/V_2^2 - p_x^2}\right), \tag{4}$$

where $p_x = \frac{\sin\alpha}{V}$ is the slowness vector of the ray in Cartesian coordinates (spherical effects for the depths of less than 50 km are small and can be neglected), V_1 and V_2 are the velocities right above and below Moho, respectively; H_{ref} is the constant Moho depth according to the reference model. The effect of the crustal corrections, dt_{vel}, and dt_{moho} upon the results of inversion is discussed in Section 3.2.

Parametrization of the velocity fields is performed on the basis of the algorithm developed by Koulakov (1998) and Koulakov *et al.* (2002). A certain amount of nodes is distributed within the study volume reflecting the ray density. In this study, the nodes are placed at 16 horizontal levels from 10 to 750 km depth. The nodes are distributed on each plane along parallel lines proportional to the ray density. A minimal distance between the nodes ($dS^{min} = 30$ km) is set to avoid excessive concentrations of them in the areas with density fluctuations. The number of the nodes in each circular area is about 7000–9000 for the P model and 5000–7000 for the S model. Eight nodes control each point of the study area and the velocity distribution is approximated using a bilinear interpolation. This parametrization might bias the resulting model due to the operator-induced orientations of the lines where the nodes are distributed. In order to avoid this problem we have performed separate inversions for two differently oriented grids: 0° and 45°. Summation of the resulting models removes most of the artefacts related to the grid orientation.

The first derivative matrix A, which reflects the effect of velocity variations at the ith node on the traveltime of the jth ray, is computed
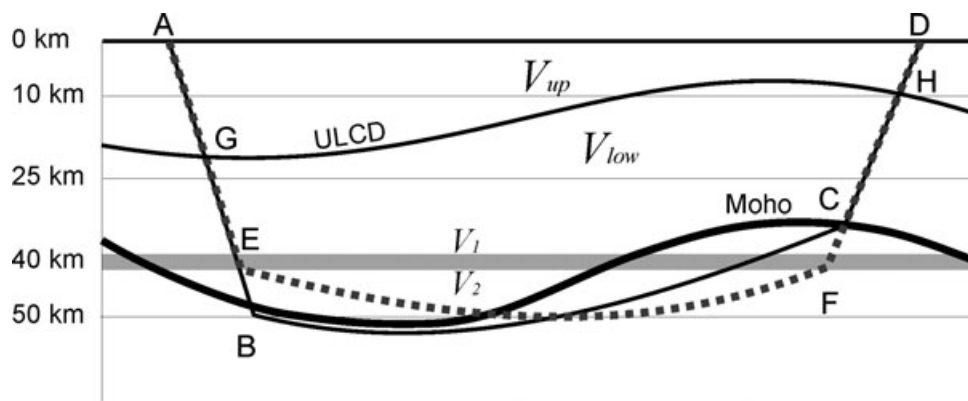
Figure 3. Simplified schemes illustrating the crustal correction. UCLD is the upper/lower crust discontinuity. The ray path ABCD (solid line) represents the real ray, which travels below the Moho interface with varied depth. In our model it is replaced by the ray path AEFD (dotted line), which corresponds to a 1-D model. Time corrections for the segments EB and FC are computed using eq. (4). V_1 and V_2 are the velocity values in the 1-D model just above and below the referenced Moho, respectively. V_{up} and V_{low} are the velocity values in the upper and lower crust according to the EuCRUST-07 model. They are used for correction of the velocity distribution in the crust according to [2]. Thin lines at depths of 10, 25 and 50 km mark the levels where parametrization nodes were located.

A. Moho depth

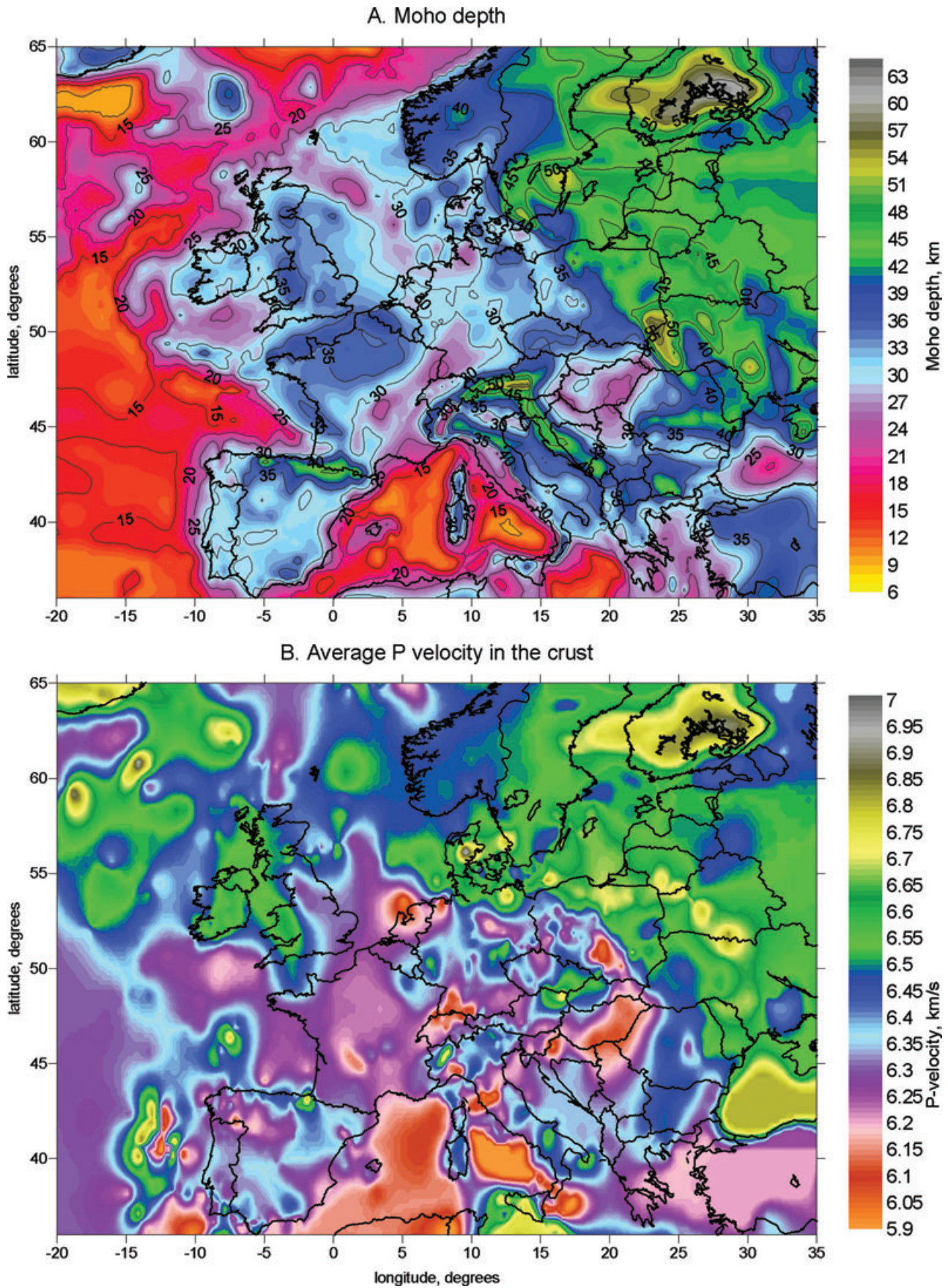

B. Average P velocity in the crust

Figure 4. (a) Moho depth (km). (b) Average crustal *P* velocity (km s^{-1}), according to the reference crustal model EuCRUST-07 (Tesauro *et al.* 2008).

by integration along the ray path γ as

$$A_{ij} = \frac{\int_\gamma \Delta g_j(\gamma)\,\mathrm{d}S}{\Delta\sigma_j}, \tag{5}$$

where Δg_j is the slowness perturbation at the current point of the ray caused by unit slowness anomaly $\Delta\sigma_j$ at the jth node. Together with the unknown P- and S-velocity anomalies, the matrix includes the elements for corrections of the source parameters (four for each source) and station corrections. We separate the cases of the station corrections when the stations are located inside and outside the study area.

Smoothing of the resulting velocity anomalies is controlled by the additional matrix block. Each line in this block contains two non-zero elements with opposite sign, corresponding to neighbouring nodes in the model. Increasing weights of these elements produces a smoothing effect upon the resulting anomalies. Determination of all the coefficients in the matrix is performed using a synthetic modelling.

The resulting matrix is inverted using the LSQR method (Paige & Saunders 1982; van der Sluis & van der Vorst 1987). The variance reduction for P-residual times is $\sim$40 per cent, while for S data it is only $\sim$25 per cent. This result demonstrates that the noise level in the S-traveltimes is significantly higher than in the P-traveltimes.

2.3 Crustal model

As previously stated, the crustal time correction was performed according to the EuCRUST-07 model (Tesauro *et al.* 2008). This new 3-D crustal model for Western and Central Europe and surrounding areas (35°N–71°N, 25°W–35°E) has been constructed using several hundred seismic profiles and receiver functions results (nearly all published data) and about 20 local compilations of the main crustal boundaries, basement and Moho depth. All the data were analysed and cross-checked to select the most robust. Finally, they were interpolated using a standard kriging method.

EuCRUST-07 offers a starting point in any kind of numerical modelling, when it is necessary to resolve a trade-off between crustal and mantle effects. The digital model, presented on a uniform $15' \times 15'$ grid, consists of three layers: sediments and two layers of the crystalline crust. This division has been chosen since at least two layers within the crystalline crust are detected in most seismic sections. In the areas, where the crystalline crust consists of only one layer with a constant velocity (e.g. in the Tyrrhenian Sea) or characterized by a gradual change (e.g. in the western part of the Black Sea), the crust is arbitrary divided in two layers of equal thickness having average velocities consistent with the seismic data. In the opposite case, several layers are jointed to form one equivalent layer, like in the East European Platform (EEP), where the velocity in the upper layer is calculated as a weighted average of upper- and middle-crustal velocities. Therefore, each layer of the crystalline crust is characterized by average V_p velocities, which are consistent with the available seismic determinations. The velocity structure of the sediments is not specified since the strong heterogeneity (both lateral and vertical) of this layer makes it hardly possible to integrate relative sparsely published data into a unified model for such a large region. On the other hand, seismic tomography results are mostly biased by crystalline crust heterogeneity whereas the upper crust effect can be more easily separated from the mantle one, as it is demonstrated by the above-mentioned tests.

The new model (Figs 4a and b) demonstrates large differences with existing regional/global compilations, mostly resulting from

inclusion of recently acquired seismic data and detailed local compilations of principal crustal boundaries. For example, we observe significant differences in the Moho depth with CRUST2.0 (Bassin *et al.* 2000), which is commonly used in seismic tomography studies. EuCRUST-07 shows a Moho 5–10 km deeper in the orogens (e.g. the Eastern Alps and the Cantabrian Mountains), reflecting a downward flexure of the subducting plate and shallower (5–10 km) in Western Anatolia and in the basins that experienced Neogene extension (e.g. the Tyrrhenian Sea). Also differences between EuCRUST-07 and another recent Moho depth compilation (Kaban 2001) are quite large, spanning from –14.9 to 17.2 km. Many principal differences are also observed in the depth to basement and crustal velocities. Differently from CRUST2.0, which shows only first order differences among a few tectonic units of the region, EuCRUST-07 demonstrates a very complex velocity structure of the crystalline crust with pronounced lateral changes.

3 INVERSION RESULTS AND VERIFICATION

3.1 Inversion of the real data

The resulting models of P- and S-velocity anomalies are shown in the horizontal sections in Figs 5 and 6. In Fig. 7, the velocity model is represented in 12 vertical sections crossing the main European structures. As was mentioned above, the presented models are the result of the separate inversions in the 12 overlapped circular windows. For each window two models were computed using differently oriented grids. Finally, the velocity is computed as weighted average

$$\mathrm{d}V^{\mathrm{sum}} = \frac{\sum_{i=1}^{N} C(d^{\mathrm{cen}})D(d^{\mathrm{node}})\mathrm{d}V_i}{\sum_{i=1}^{N} C(d^{\mathrm{cen}})D(d^{\mathrm{node}})}, \tag{6}$$

where N is the number of the models (24, in our case); C is the weight function depending on the distance from the centre of the current model (for the distances up to $R/2$, where R is the radius of the current area, $C = 1$; for the distances from $R/2$ to R the value of C decreases linearly from 1 to 0); D depends on the distance to the nearest parametrization node. The values of the velocity anomalies are given only if the distance to the nearest node is less than a predefined value d^{min} (40 km, in our case). As already stated, the parametrization nodes were installed according to the ray density. We have used a fairly conservative way for the node installation. Consequently, the results are only shown in the areas where the data amount provides a satisfactorily robust solution. A more detailed description of the obtained anomalies is provided in Section 4, after showing the synthetic reconstructions.

3.2 Effect of the crustal corrections

As discussed in the introduction, the impact of the crust on the upper-mantle velocity anomalies detected by tomography can be quite significant (e.g. Martin *et al.* 2005, 2006). To estimate the effect of the crust on the results of real data inversion, we have performed the inversion without the crustal corrections. All other parameters are the same as for the case of computing the main model presented in Figs 5–8. P-velocity anomalies obtained in this case are shown in the left-hand column of Fig. 8. We compare this model with the main results and present the differences of the P-velocity models with and without crustal corrections (Fig. 8, right-hand column). The maximum difference is observed
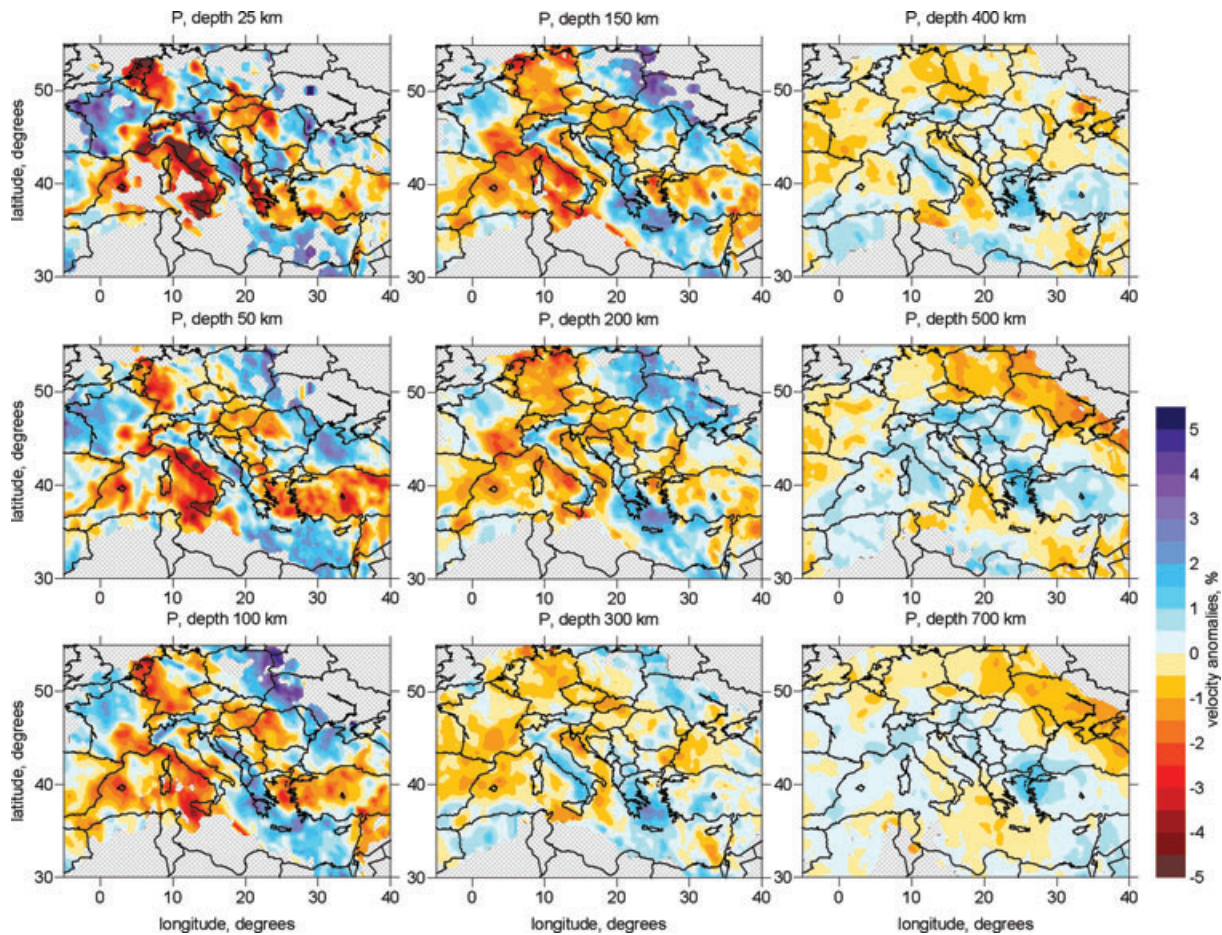
Figure 5. Inversion results for *P*-velocity anomalies in the upper mantle in horizontal sections.

at 25 km depth, and it is absolutely coherent with variations of the Moho depth and crustal velocities according to EuCRUST-07 (Fig. 4). At 50 km depth, the differences are also significant and reach ±1.7 per cent, which is about 45 per cent of the total anomaly amplitude. At a greater depth the influence of the crustal correction tends to decrease, producing differences of about ±1 per cent (~25 per cent of total anomaly amplitude) at 100 km approximately at the same places as above. The effect of the crust still present at 150 km is already within the determination error in most of the study area and becomes slowly negligible (<0.5 per cent) in the deeper layers.

3.3 Test with odd and even numbers of events

We can observe from the rather low variance reduction (from 30 to 40 per cent) in the inversion that the noise level in the data is significant. In this case, the key test that allows us to estimate the contribution of the random noise is the reconstruction with odd and even data. This test implies a random separation of the entire data set into two subsets (e.g. with odd and even numbers of rays) and their independent inversion.

The processing algorithm and free parameters for the grid construction and inversion are the same as in the case of the inversion of the entire data set. In our experience, we found some cases in which this test has provided non-coherent solutions due to a too high-noise level (e.g. for the *S* model in the Pamir-Hindukush area, Koulakov & Sobolev 2006). In these cases the traditional tests (e.g. checkerboard test) did not show the real quality of the data. By

contrast, the odd/even test provides very important supplementary information and should be performed in any tomographic study.

Inversion results for the halved *P* and *S* data sets are shown in Fig. 9. The models can be compared with each other and also with the results obtained using the entire data set (Figs 5 and 6) to show the effect of data halving on the inversion results. It can be observed that both *P* and *S* model show an almost perfect correlation between the maps at corresponding depths. For the shallow levels, even small patterns of anomalies (less than 100 km of lateral size) are similarly presented in all maps. As this test demonstrates that the fairly strong noise presented in ISC data does not influence significantly the inversion results, it supports the consistency of the obtained velocity models.

3.4 Sensitivity tests

The synthetic modelling was performed within the framework of the linear model. This means that the synthetic residuals were computed along the ray paths traced in the 1-D spherical model. As previously discussed, the performance of the full 3-D ray tracing would require a very long computation time, which would obviously limit the number of the tests. In our opinion, the advantages of fast calculations performance fully compensate the shortcomings related to the negligence of the non-linear effect.

The same source/receiver pairs as in the real data inversion were used to compute synthetic residuals. The random noise with the statistical distribution having the same shape of the residuals distribution in the ISC catalogue was added to the synthetic residuals.
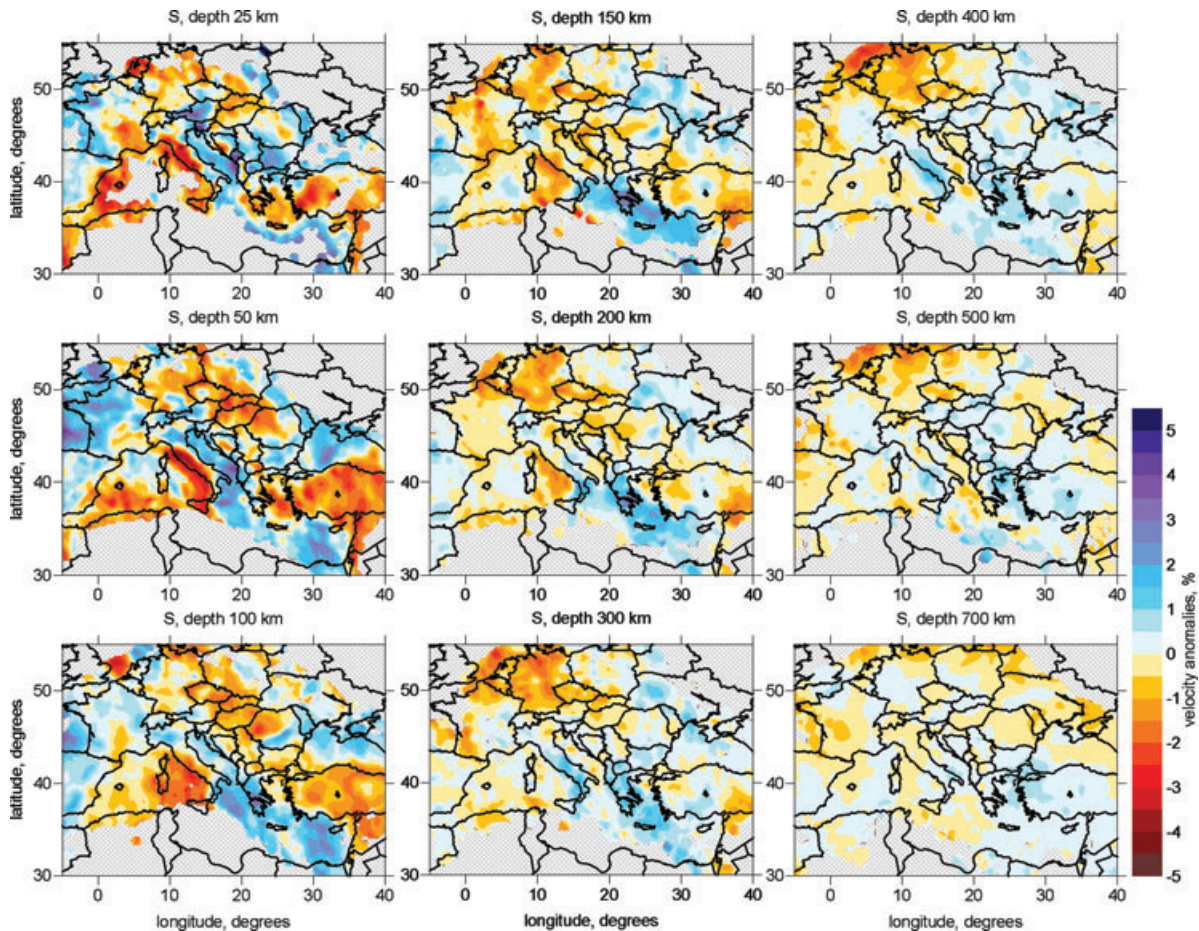
Figure 6. Inversion results for *S*-velocity anomalies in the upper mantle in horizontal sections.

The amplitude of noise was defined separately for *P* and *S* data in order to obtain the same value of variance reduction after synthetic inversion as in the real data case. It should be noted that the noise level defined according to this criteria depends on the anomalies configuration. For the smaller synthetic anomalies the defined noise level is weaker. Therefore, for the *P* model, with checkerboards of size 1° and 2° the noise level is equal to 0.3 and 0.4 s, respectively. In case of the *S* model with patterns of a size 2° and 3°, the noise level is equal to 0.6 and 0.8 s. A reconstruction of the model was performed using the same algorithm and with the same free inversion parameters as in the real-data case.

The checkerboard tests with horizontal resolution are shown in Figs 10 and 11. The synthetic models are represented by alternated cells with amplitudes of anomalies of ±3 per cent. In all cases, the sign of the anomalies changes in the vertical direction at 200, 400 and 600 km depth. We present the models, which correspond to two different runs of a simultaneous reconstruction of the *P* and *S* models. In the first case we reproduced the checkerboards with the lateral size of 1° × 1°, for the *P* model and 2° × 2° for the *S* model. In the second run, we employed the cell size of 2° × 2°, for the *P* model, and 3° × 3°, for the *S* model. The amplitudes of the anomalies in all presented tests are equal to ±3 per cent. The reproduced images can be used to estimate a capacity of the algorithm in retrieving fixed size anomalies. According to our experience, when small-scale anomalies are reliably restored, the larger patterns will be restored with the same or better quality. In addition, the checkerboard tests give the chance to identify the

areas of possible smearing due to uneven azimuthal distribution of the rays. The checkerboard tests for the *P* model show a relatively high-horizontal resolution for most of the European region, while for the *S* model there are areas lacking resolution (e.g. beneath France). In these areas the amount of the *S*-wave teleseismic rays is not sufficient to retrieve any relevant information.

The vertical resolution has been investigated using the vertical checkerboard tests (Fig. 12). The synthetic model has been produced for seven cross-sections, which were used to present the main results. Fig. 13(a) gives an overview of the initial and reconstructed model at the depth of 100 km. It can be observed that the synthetic anomalies are defined along the sections as horizontal alternated blocks. The shapes of the initial patterns and the reconstructed anomalies are shown in seven profiles in Fig. 13(b). In the present example, the size of anomalies is 100 km × 100 km for the *P* model and 200 km × 200 km for the *S* model. A random noise with the rms of 0.3 and 0.6 s for *P* and *S* data, respectively, was added. The results of this test show that in most parts of the study area the synthetic patterns are satisfactorily reconstructed for both the *P* and the *S* data, which confirms a rather good vertical resolution.

3.5 Model with realistic configurations of anomalies

Fig. 13 shows a synthetic model, which was used to reproduce the results similar to the real data inversion. Velocity anomalies are defined in a set of vertical prisms limited by two depth levels.
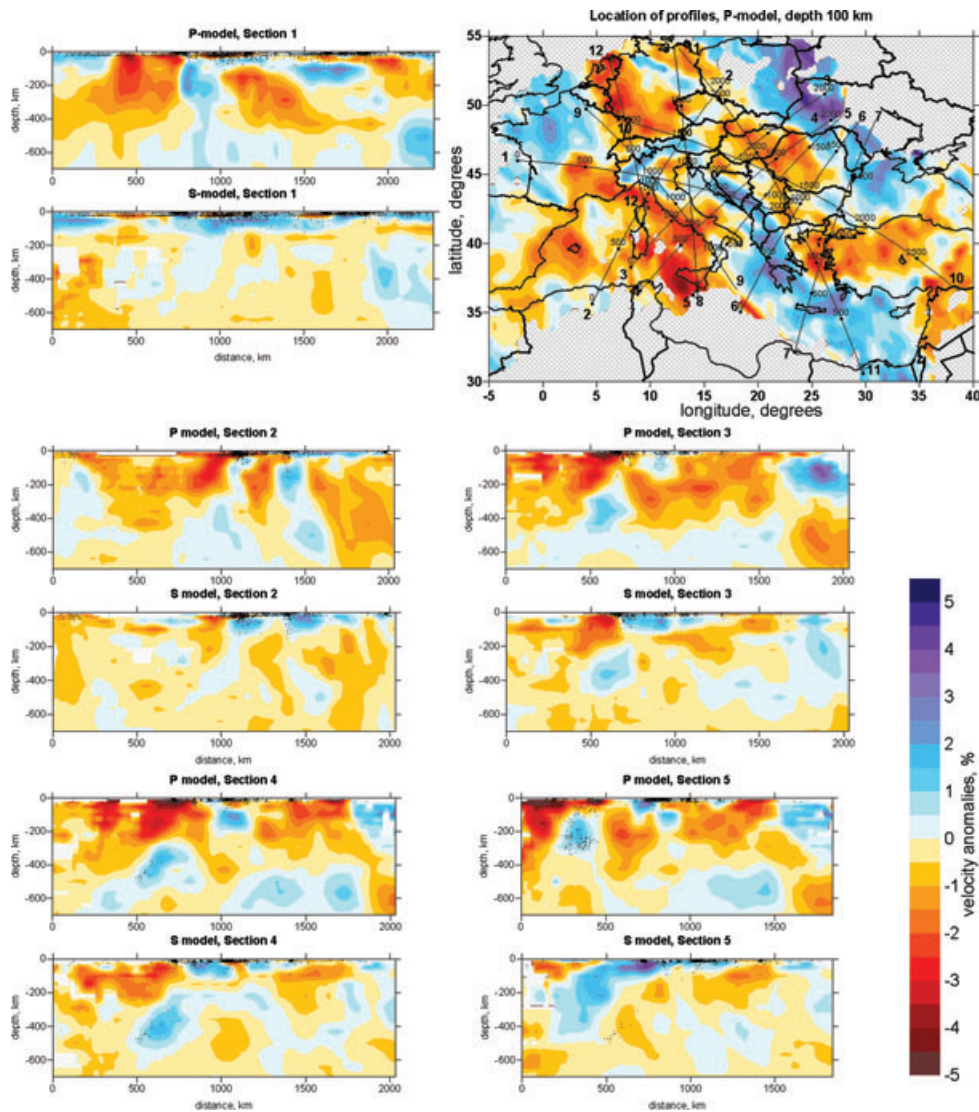
Figure 7. Resulting *P*- and *S*-velocity anomalies in 12 vertical sections. Positions of the cross-sections are shown in the map view on the right side. Black points in sections represent the distribution of relocated events at distances less than 100 km from the profile.

Using these prisms we can create any complex 3-D pattern. Shape and amplitude of the synthetic anomalies are modified to obtain maximum similarity with the real data inversion. This operation is performed iteratively by a trial and error method and takes a long computation time. Therefore, we solve the forward and inverse problems until the required similarity is retrieved. The residuals computed during the forward modelling are perturbed by noise. The value of the noise is determined to obtain approximately the same value of variance reduction after inversion as in the case of the real data inversion. The noise was created by a random noise generator, which has a statistical distribution of the same shape as the residuals distribution in the real data set. In this model we defined the noise at 0.5 and 1 s for the *P* and *S* residuals, which resulted in a variance reduction of ∼40 and 25 per cent for the *P* and *S* data correspondingly. In this way, the synthetic model obtained should represent the real situation.

The results of this modelling make it possible to obtain a fair estimation of the amplitudes of the seismic anomalies in the Earth. The latter are usually rather uncertain in the existing tomographic models, due to a dependence of the inversion results on regularization and smoothing parameters, strongly affecting the amplitudes of the solution. Although there are several known attempts to formalize a selection of these parameters (e.g. using the trade-off curves), an unambiguous way to determine the damping coefficients probably does not exist yet. Indeed, their values depend on a great number of data, parameters and factors (e.g. noise level; configuration of the observation system). In addition, in many tomographic studies, especially at a regional scale, there is a strong disproportion of the ray distribution. In this case, one set of the regularization parameters can result in an underdamped solution in one part (with denser ray distribution) and overdamped solutions in other parts (with sparse ray coverage). Therefore, in most tomographic studies the amplitudes, obtained after inversion of real data, might not reflect real values of the anomalies in the Earth. Performing synthetic modelling with realistic shapes and amplitudes of the anomalies, as proposed in this section, allows for a more direct assessment of the combined effect of damping and ray illumination on realistic anomalies.

Let us assume that X_0 is the real velocity distribution in the Earth. The rays travelling through this velocity anomaly produce
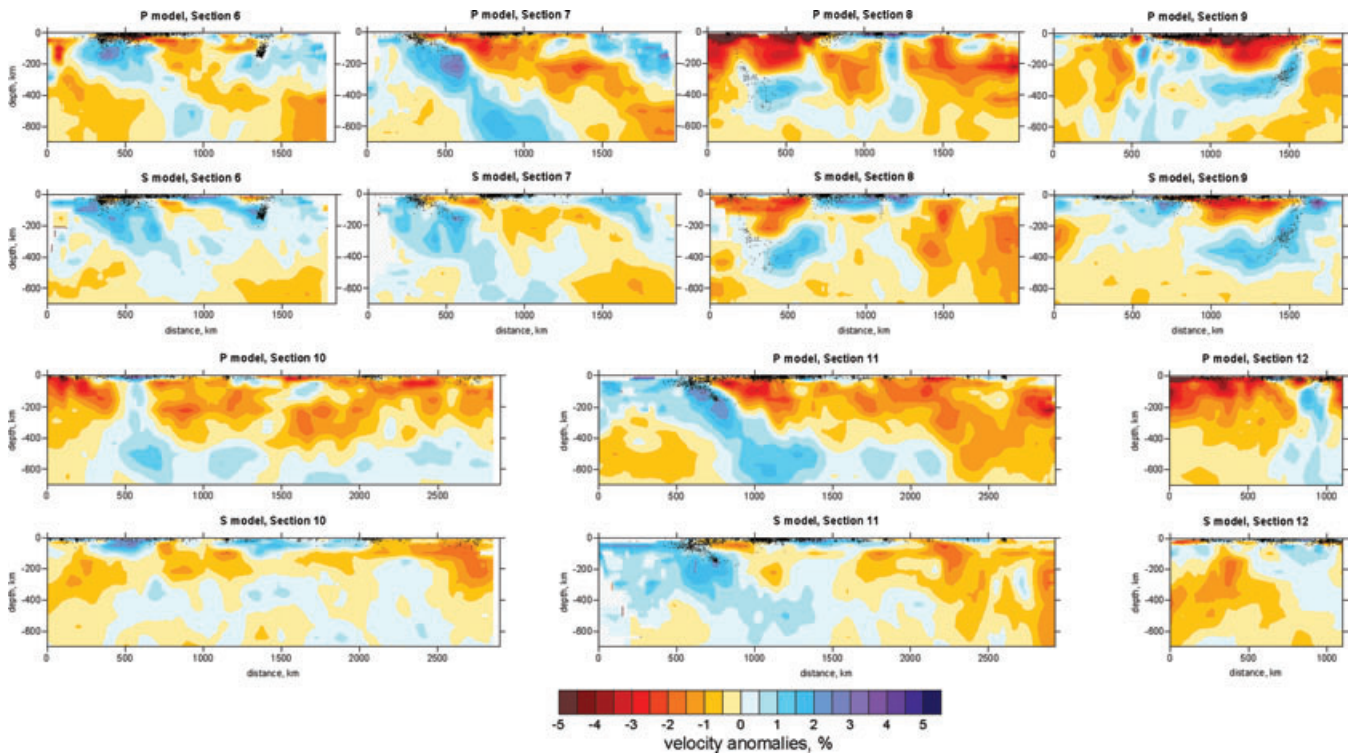
Figure 7. (*Continued.*)

the real data set D_0. Performing the inversion with a set of the free parameters (S_0) produces the resulting model X_1. As previously stated, deviations of the anomalies in the obtained model ($\|X_1\|$) are not necessarily the same as $\|X_0\|$, due to uncertainty of the free parameters and disproportion of the ray distribution. In the test shown in Fig. 13 we create the synthetic model X_2, which is used to compute the data set D_2. After performing inversion for these data with the same set of free parameters (S_0) as in the real data inversion, we obtain the model X_3, which is approximately equal to X_1. Since the inversion conditions are absolutely identical, we can assume that X_0–X_2. This approach has already been successfully employed to estimate real velocity perturbations in the mantle beneath the Dead Sea region based on teleseismic data (Koulakov *et al.* 2006). It should be noted that the values in the synthetic model X_2 are not necessarily the same as in the recovered model X_3. Therefore, in geophysical studies requiring employment of tomography data to infer values of temperature, composition, and other petrophysical parameters, it is recommended to use the amplitudes given in the synthetic model rather than in the real inversion results. Therefore, the description of patterns presented in the next section is based on a joint analysis of the real data results and the recovered synthetic model.

4 STRUCTURE OF THE UPPER MANTLE

The real inversion results and the recovered synthetic model for the *P*- and *S*-velocity anomalies beneath Europe are presented in Figs 5, 6 and 13. A number of vertical sections showing velocity distributions are displayed in Fig. 7. Despite applying the crustal correction, the amplitudes of the velocity anomalies remain significant in the uppermost layers of the model. The initial crustal model is well constrained in most parts of the study area. It is also clear, that the reproduced crustal anomalies correlate well with the anomalies in the uppermost mantle. Therefore, it appears that a substantial

smearing of the mantle anomalies into the crust still takes place. Possible reasons for this could be the same as for the propagation of the Moho effect into the crust, as previously described. We leave this problem for future studies and concentrate on the velocity structure of the upper mantle at depths of 50–700 km.

4.1 Large-scale features of the mantle structure

On a large scale, main features are observed in both *P* and *S* model from the top of the upper mantle down to at least 300 or even 400 km. Their similarity is particularly clear in the depth range between 50 and 200 km, where the resolution of the *S* model is sufficient. One of these features is the sharp transition occurring along the Trans European Suture zone (TESZ; cross-sections 3, 4, 5, 6 and 7) from the negative anomalies (up to −4 per cent), characterizing the young tectonic features of Central Western Europe, to the positive anomalies found beneath the Palaeozoic East European Platform (EEP; ∼2 per cent). Along this area an abrupt change of all geophysical parameters of the European lithosphere is observed (e.g. Kaban 2001; Artemieva *et al.* 2006; Tesauro *et al.* 2007; Kaban *et al.* 2009). The pattern of the large-scale anomalies is in general consistent with the results of previous tomographic studies (e.g. Snieder 1988; Spakman *et al.* 1993; Zielhuis & Nolet 1994; Marquering & Snieder 1996; Curtis *et al.* 1998; Martinez *et al.* 2000; Piromallo & Morelli 2003; Marone *et al.* 2004). However, these studies yielded remarkably different depth extensions of the above-mentioned structures. Some of the models (e.g. Piromallo & Morelli 2003) observe these anomalies (e.g. beneath the TESZ) extending up to 350–400 km, while others do not reveal them at depths greater than 200 km (e.g. Zielhuis & Nolet 1994) or 300 km (e.g. Marquering & Snieder 1996). Our results demonstrate that these anomalies, more pronounced in the *P* model, extend up to 300 km and become very weak at greater depths (Fig. 7, cross-section 12). Furthermore, at the depth interval of 300–400 km we
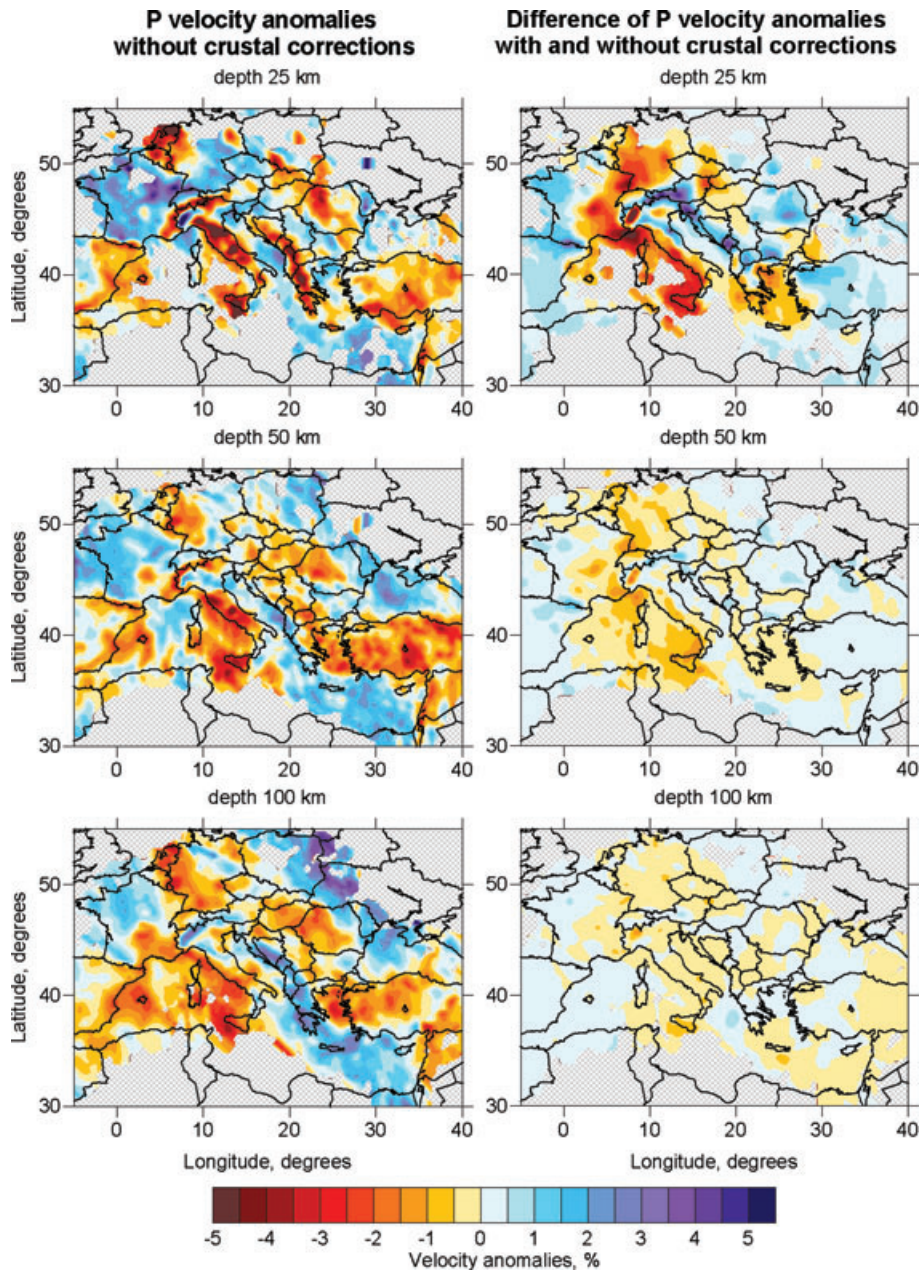
Figure 8. Study of the effect of the crustal corrections. Left column shows results of inversion for *P*-velocity anomalies without including crustal corrections. Right column shows difference between *P*-velocity anomaly models obtained for the cases of data with and without crustal corrections.

can observe in the *P* model that the velocity contrast across the TESZ (transition to higher velocities) is shifted to the east beneath EEP with respect to the shallower mantle. By contrast, in the *S* model at the same depth range, the positive anomalies tend to be dominant also in Western Europe (Figs 5 and 6).

The deepest layers (400–700 km) in both *P* and *S* models show a broad positive anomaly (between 0.5 and 2 per cent) below most parts of Southern Europe. Some of these larger-scale high-velocity structures can be interpreted as remnants of the Tethyan oceanic lithosphere (e.g. Piromallo & Faccenna 2004; Schmid *et al.* 2006; Vignaroli *et al.* 2008). In some areas they are connected with the anomalies in the upper mantle. This is, for instance, the case for the fast anomalies underneath the Northern Aegean, the Alps and the Calabrian Arc. Under these structures we observe the slabs subducted down to the transition zone (TZ; e.g. below the

Calabrian arc) or even to the lower mantle (below the Aegean plate), which in some cases tend to join in a single high-velocity body (e.g. the Eurasian plate descending below the Western Alps and the Adriatic plate subducted under the Calabrian arc, cross-section 9 of the *P* model). At these depths the anomalies of the *S* model are less pronounced than in the *P* model, on account of the loss of resolution.

4.2 Regional structure of the upper mantle (a general overview)

On a smaller scale, positive *P*-velocity anomalies in the upper mantle are typical for several basins. In the Adriatic, Ionian and Po basins the fast velocities (2 per cent) are observed only in the uppermost layer (~50 km), while in some other places they extend to depths of
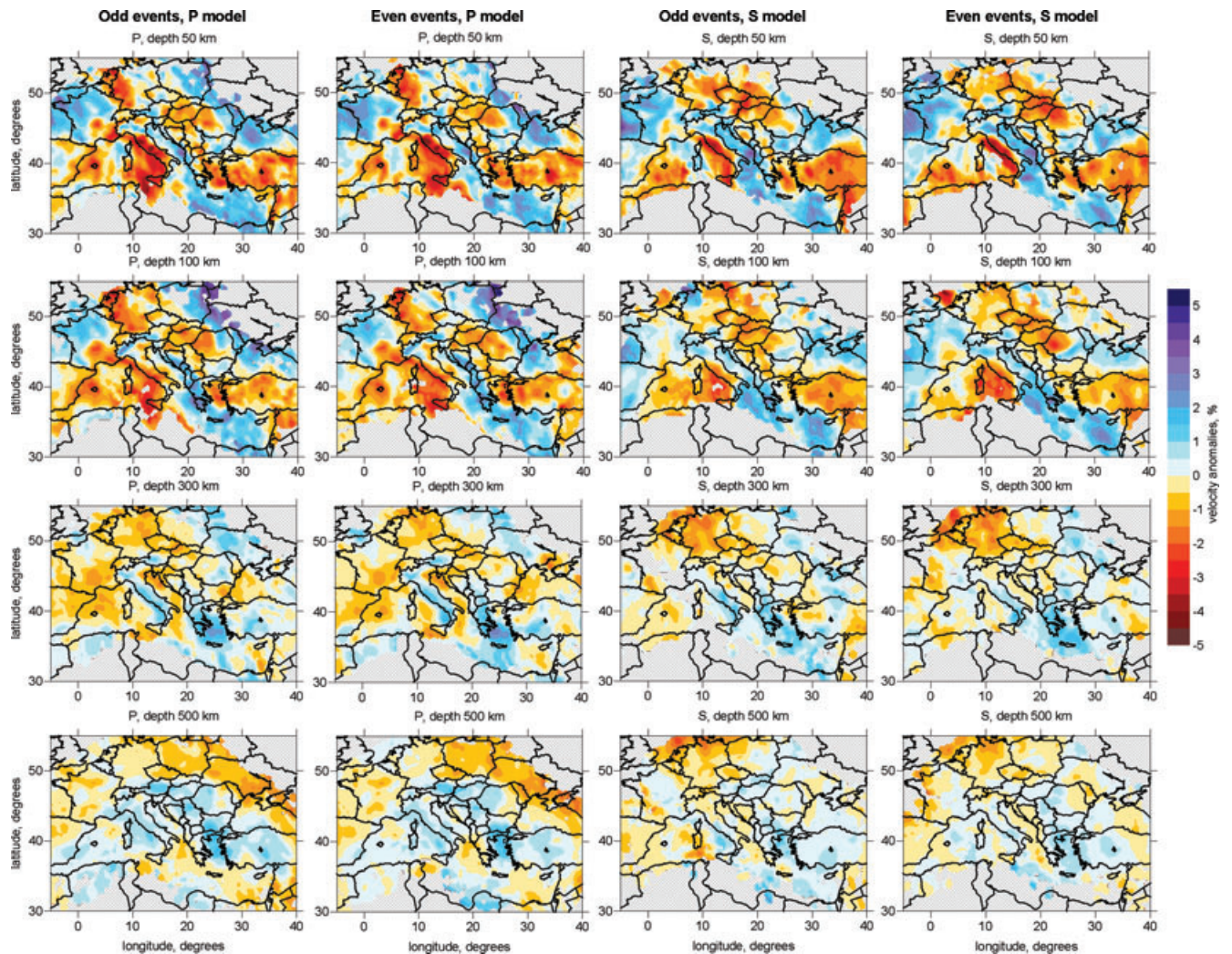
Figure 9. Test for the inversion of two independent data subsets (with odd/even numbers of events). *P*-wave anomalies are compared in the first two columns on the left side, while *S*-wave anomalies are compared in the first two columns on the right side. The results are presented for four depth levels.

150–200 km (e.g. in the Aquitaine and Paris Basin and in the Black Sea). The presence of high-velocity structures in these areas is also in agreement with high *Pn* values detected in several studies (e.g. Mele *et al.* 1998; Hearn 1999; Al-Lazki *et al.* 2004). In more detail, below the Black Sea our model shows fast anomalies confined to its central and western parts. This could be an indication for a cold consolidated lithosphere, which is in agreement with extremely low surface heat flow (30–40 mWm^{-2}, see Galushkin *et al.* 2006).

Negative *P*-velocity anomalies (between −2 and −4 per cent) are normally confined to the Neogene backarc regions (as the Alboran, the Tyrrhenian and the Aegean Sea, the Valencia Trough and the Pannonian Basin), magmatic provinces (e.g. volcanic provinces of central Italy) and the Anatolian Plateau (cross-sections 2, 3, 4, 7, 8, 10 and 11). They are especially pronounced in the uppermost mantle down to ∼200 km and extend with a reduced amplitude to ∼300 km. These results are similar to previous *P*-wave tomography models (e.g. Spakman *et al.* 1993; Piromallo & Morelli 2003), although the amplitudes are often remarkably different. They are also in agreement with the low *Pn* values (∼7.6–7.9 km s^{-1}), observed by Mele *et al.* (1998), Hearn (1999), Webér (2002) and Al-Lazki *et al.* (2004) and seismic refraction models (e.g. Hatzfeld & the Working Group for Deep Seismic Sounding 1978; Šroda *et al.* 2006). Furthermore, these areas are mostly characterized by a very

high-heat flow of about 120 mW m^{-2} in the Pannonian basin (Lenkey 1999) and the Alboran sea (Polyak *et al.* 1996) and >200 mW m^{-2} in the Tyrrhenian sea and in the Anatolian plateau (Zito *et al.* 2003; Hurtig *et al.* 1992). The residual gravity mantle anomalies demonstrate similar negative patterns for the above-mentioned areas (e.g. Kaban 2001; Tesauro *et al.* 2007; Kaban *et al.* 2009). All these factors point to a thermal origin of the negative velocity anomalies in the backarc regions, possibly accompanied by partial melting and reduced lithosphere thicknesses (between ∼70 km in the Anatolian Plateau see Goek *et al.* 2007 and ∼30 km in the Tyrrhenian Sea, see Calcagnile & Panza 1990). In several places we observe inversion of the sign of the anomalies with depth. As an example, the negative anomaly beneath the Alboran Sea, observed at shallow depth (50–100 km), becomes positive in deeper layers (at ∼100 and ∼150 km in the *S* and *P* model, correspondingly) and tends to extend to the Balearic Sea and the Betics. These trends might be interpreted as the image of a subducted slab (e.g. Gutscher *et al.* 2002) or delaminated lithospheric material (Calvert *et al.* 2000). Since this structure is close to the western edge of the study area we do not have enough resolution to discriminate between these hypotheses.

Other pronounced low velocity anomalies (up to −4 per cent) with a size of ∼100 km are observed beneath the Massif Central
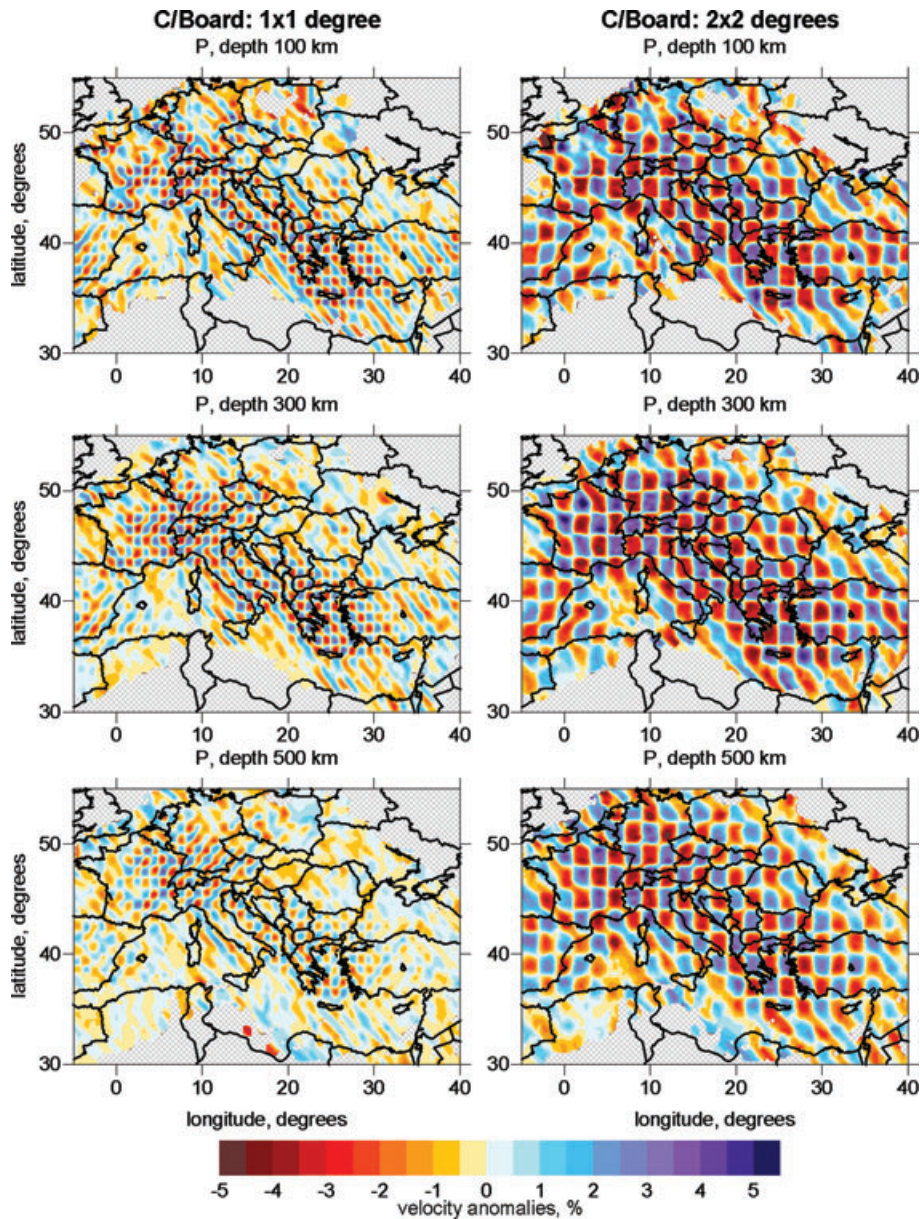
Figure 10. Reconstruction results for two checkerboard models for checking the horizontal resolution of the *P* model. The synthetic models are represented by alternated cells with an amplitude of the anomalies of ±3 per cent. Horizontal size of anomalies is $1° \times 1°$ (left-hand panel) and $2° \times 2°$ (right-hand panel). The sign of anomalies changes at 200, 400 and 600 km depth. A random noise of 0.3 and 0.4 s amplitude is added in the first and second case, respectively.

(cross-section 1) and the Rhenish Massif (cross-section 12) from the top of the mantle up to a depth of ∼300 km. In the depth range from 100 to 200 km these anomalies coalesce into a broad negative zone (between −1 and −3 per cent) underneath the Tyrrhenian Sea, the European Cenozoic Rift System (ECRIS) and extend to the east in the Bohemian Massif. These results are in agreement with previous studies. However, remarkable differences with the existing models are observed in the Eifel region (Rhenish Massif). Keyser *et al.* (2002) and Ritter (2007) have found that the low velocities extend down to at least 400 km, hypothesizing a source of this anomaly in the TZ/lower mantle. However, we observe the strong low velocity anomaly (−4 per cent) down to ∼250 km in the *P* model and a little bit deeper in the *S* model (−2 per cent) (cross-section 12). Differently from a recent regional study (Keyser *et al.* 2002; Ritter 2007), the anomaly imaged by the *S* model does not show any interruption at the mid of the upper mantle. In both mod-

els this anomaly extends to the top of the TZ, but with a reduced amplitude (−1 per cent). In the Eger Tertiary graben (Bohemian Massif) a low velocity zone (−2 per cent) is observed in both *P* and *S* models, but only in the uppermost mantle between ∼80 and ∼250 km (cross-section 8), which leaves the question about the presence of a hypothetical plume at greater depths (Plomerová *et al.* 2007) still open.

Compared to the *P* model, the *S* model more clearly shows a continuous extension of the positive anomalies characterizing the Po plain, the Adriatic and the Ionian Sea to a depth of about 100 km. These findings confirm the hypothesis of a cold and high-density domain in the uppermost mantle (e.g. Tesauro *et al.* 2007; Kaban *et al.* 2009), considered as a wedge of the African plate (e.g. de Jonge *et al.* 1994). Furthermore, the *S* model with respect to the *P* model more sharply marks at a depth of 50 km the transition from positive to negative anomalies from the Black Sea southward
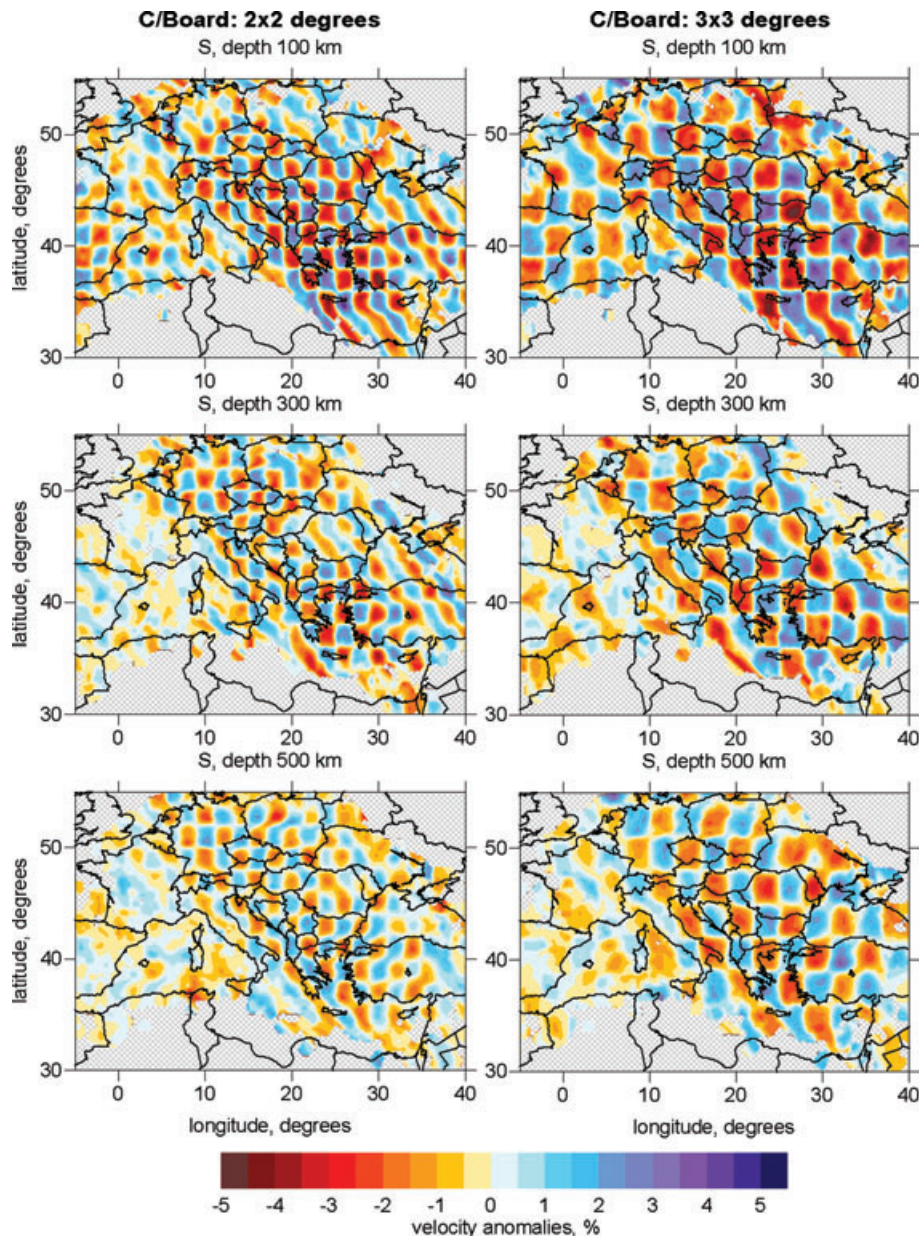
Figure 11. Reconstruction results for two checkerboard models for checking the horizontal resolution of the *S* model. The synthetic models are represented by alternated cells with amplitude of anomalies of ±3 per cent. Horizontal size of anomalies is 2° × 2° (left-hand panel) and 3° × 3° (right-hand panel). The sign of anomalies changes at 200, 400 and 600 km depth. The random noise of 0.6 and 0.8 s amplitude is added in the first and second case, respectively.

to the Anatolian plateau and from the Adriatic and Ionian sea westward to the Apennines, possibly reflecting an abrupt temperature change.

4.3 Alps, Apennines and Calabrian arc

Below the western and central Alps the fast V_p anomaly (2 per cent) is particularly pronounced from 100 km down to 300–350 km. It is usually interpreted as the Eurasian lithosphere subducted below the Adria plate (e.g. Lippitsch *et al.* 2003; Piromallo & Morelli 2003). The northwestern transition from this high-velocity structure to the low-velocity zone (−2 per cent) characterizing the ECRIS is quite sharp. Cross-sections 1 and 9 of the *P* model clearly image the Eurasian plate descending below the Adriatic lithosphere in a SE direction (cross-section 1) up to a depth of ∼300 km. On the other

hand, in the *S* model the fast anomaly can be clearly traced down to ∼200 km only, without showing a clear subduction pattern, probably due to a lack of resolution.

A negative anomaly beneath the Po plain (−1.5 per cent) is clearly visible in both *P* and *S* model between 80–130 km and about 300 km. Differently from previous local studies (e.g. Lippitsch *et al.* 2003), this anomaly is more extended at a depth of ∼100 km in the *P* model. A continuous high-velocity zone is observed under the eastern Alpine chain, from ∼2 per cent at the top to ∼1 per cent at a depth of ∼300 km. This might be an image of a subducted plate (cross-sections 2, 8 and 10 of the *P* model), which is in agreement with previous studies (e.g. Lippitsch *et al.* 2003). However, the polarity of the slab remains unclear. Both the Eurasian and Adriatic plates, indeed, seem to be connected in this high-velocity body. At greater depths (>300 km) the positive anomaly attenuates
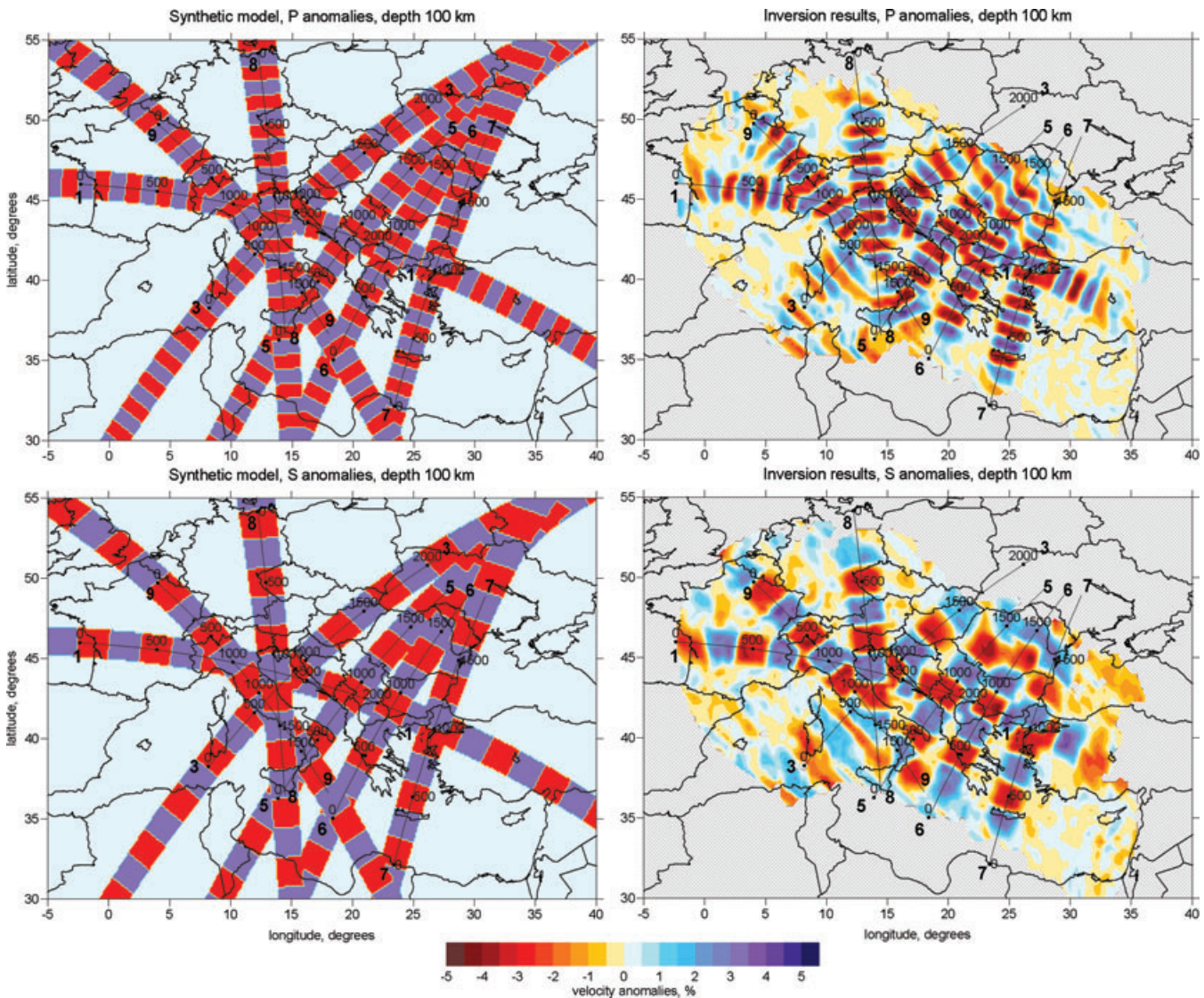
Figure 12. Checkerboard test for seven vertical sections. The synthetic model is defined as alternated horizontal blocks oriented across the vertical profiles. Level of noise is 0.3 and 0.6 s for *P* and *S* data, respectively. (a) Map view of the initial synthetic anomalies and results of reconstruction at the depth of 100 km. (b) Synthetic model and reconstructed anomalies presented in seven vertical profiles. Location of the profiles is shown in the maps in (a). Number of the profiles is the same as in Fig. 7.

(cross-sections 8 and 10) and tends to join with the fast anomaly in the TZ beneath the Apennines related to the subducted Adria plate (cross-section 8). The detailed local model of Lippitsch *et al.* (2003) has evidenced a N-dipping of the Adriatic slab in the uppermost part of the mantle down to ∼250 km. The present model images elongation in the north direction only of the deep portion (below 300 km) of the slab (cross-sections 2 and 8), which supposes plunging of the Adria plate beneath Eurasia near the TZ. This conclusion is principally different from previous studies but, on account of the poor resolution at this depth, needs further verifications. The *S*-wave model shows only a thick lithosphere (∼150 km) in this area, without a clear pattern of subduction, like in the western Alps (cross-section 2, 8 and 10).

Below most parts of the Apennines negative velocity anomalies are observed from the top of the mantle (−4 per cent) up to a depth of ∼100 km in both *P* and *S* models. At a greater depth (∼150 km) two major high-velocity structures (1 per cent) are visible beneath the northern and the extreme southern part of the chain (Calabrian arc).

At depths from 250 to 350 km a unified fast anomaly is observed below the entire belt, which joins northward the positive anomaly beneath the Alps (cross-section 9 of *P* model). This anomaly is shifted westward in the deeper horizontal sections (350–400 km). The shallow negative anomaly is usually interpreted as a part of the mantle wedge between the crust and the subducted slab (e.g. Hearn 1999), while the deeper high-velocity structure represents a signature of the subducted Adriatic lithosphere (e.g. Piromallo & Morelli 2003; Marone *et al.* 2004). The low anomalies observed in our model beneath the central southern Apennines up to a depth of ∼250 km were differently interpreted in previous studies. For instance, some authors explain this feature as a subducted promontory of the continental lithosphere (Lucente & Speranza 2001) or as a lithosphere attenuated by a hot asthenospheric wedge (Amato *et al.* 1998; Cimini & de Gori 2001). Other authors (e.g. Bijwaard & Spakman 2000) have found a gap in the same area (∼100 km wide) between the Adriatic plate and the subducted lithosphere, and interpreted it as a result of lateral migration of slab detachment
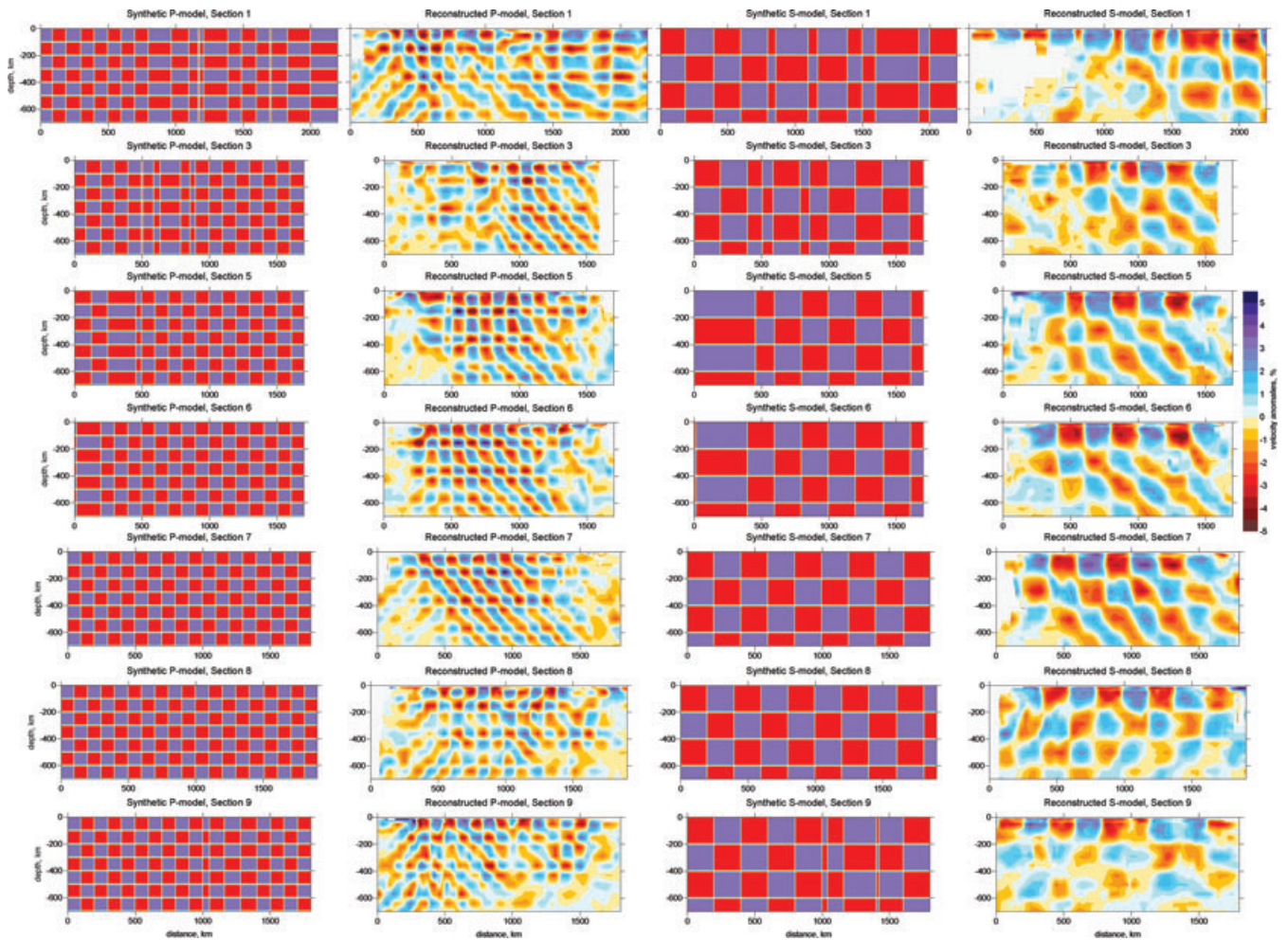
Figure 12. (*Continued.*)

from northwestern Italy to the Calabrian Arc (Wortel & Spakman 1992). We display several cross-sections (2, 3, 4, 5, 8 and 9) mostly perpendicular to the Apennines, in order to investigate the issue of the Adriatic slab continuity. It can be observed that below the northern Apennines (cross-section 2) a continuous fast body, which may be associated with the subducted plate, is imaged in the *P* model down to the top of the TZ. However, this feature is not visible in the *S* model, which only evidences a thick lithosphere (∼150 km) without pronounced anomalies at greater depths. Beneath the central Apennines (cross-sections 3, 4 and 8) the anomaly pattern is remarkably different. We have found a break of the fast velocity zone in the *P* model with increasing size (from ∼50 to ∼100 km) and depth (from 100–150 to 200–300 km) from north to south correspondingly. Beneath the Calabrian arc the continuous lithosphere slab is imaged in the *P* model (cross-sections 5 and 9) dipping to the west down to the top of the TZ, where it flattens (cross-section 9). However, this fast anomaly is attenuated between 50 and 100 km (cross-sections 4), which provides evidence for an extension of the gap detected in the central-southern Apennines to this area (Bijwaard & Spakman 2000). The deepest part of the Adriatic slab beneath the Apennines (>250 km) is imaged in all cross-sections as a whole coherent body reaching the top of the TZ. The *S* model also evidences for a gap disconnecting the slab subducted below the central-southern Apennines, but it is more attenuated (cross-sections 3, 4 and 8) and smaller in size (cross-

section 4). Furthermore, the Adriatic subducted plate is imaged as a continuous fast body below the Calabrian arc (cross-sections 5 and 9). The *S* model demonstrates similar results for this area and reaches a much higher detail relative to previous models (e.g. Marone *et al.* 2004), which usually do not show a clear pattern of subduction and loose resolution below ∼250 km. Therefore, both *P* and *S* model confirm the presence of a gap in the Adriatic slab below the central and southern Apennines, possibly extending to the Calabrian arc. This gap has been recently interpreted (Chiarabba *et al.* 2008) as a result of updoming astenospheric material along a tear, which mechanically separates the Ionian and the Adriatic slab. However, the attenuation of the negative anomaly in the *S* model evidences against the hypothesis of a pure thermal origin of this low velocity anomaly, since temperature variations would produce a stronger reduction of *S* than of *P* velocities (e.g. Goes *et al.* 1999).

4.4 Carpathians

Most of the Carpathians are underlain by fast *P* anomalies (2 per cent) from the top of the upper mantle down to about 250 km (cross-sections 5 and 6). The presence of a deep lithospheric block underneath this area is also supported by previous tomographic models (e.g. Piromallo & Morelli 2003; Marone *et al.* 2004) and other geophysical studies (e.g. Kaban 2001; Tesauro *et al.* 2007; Kaban *et al.* 2009). However, the new *S* model distinguishes fast
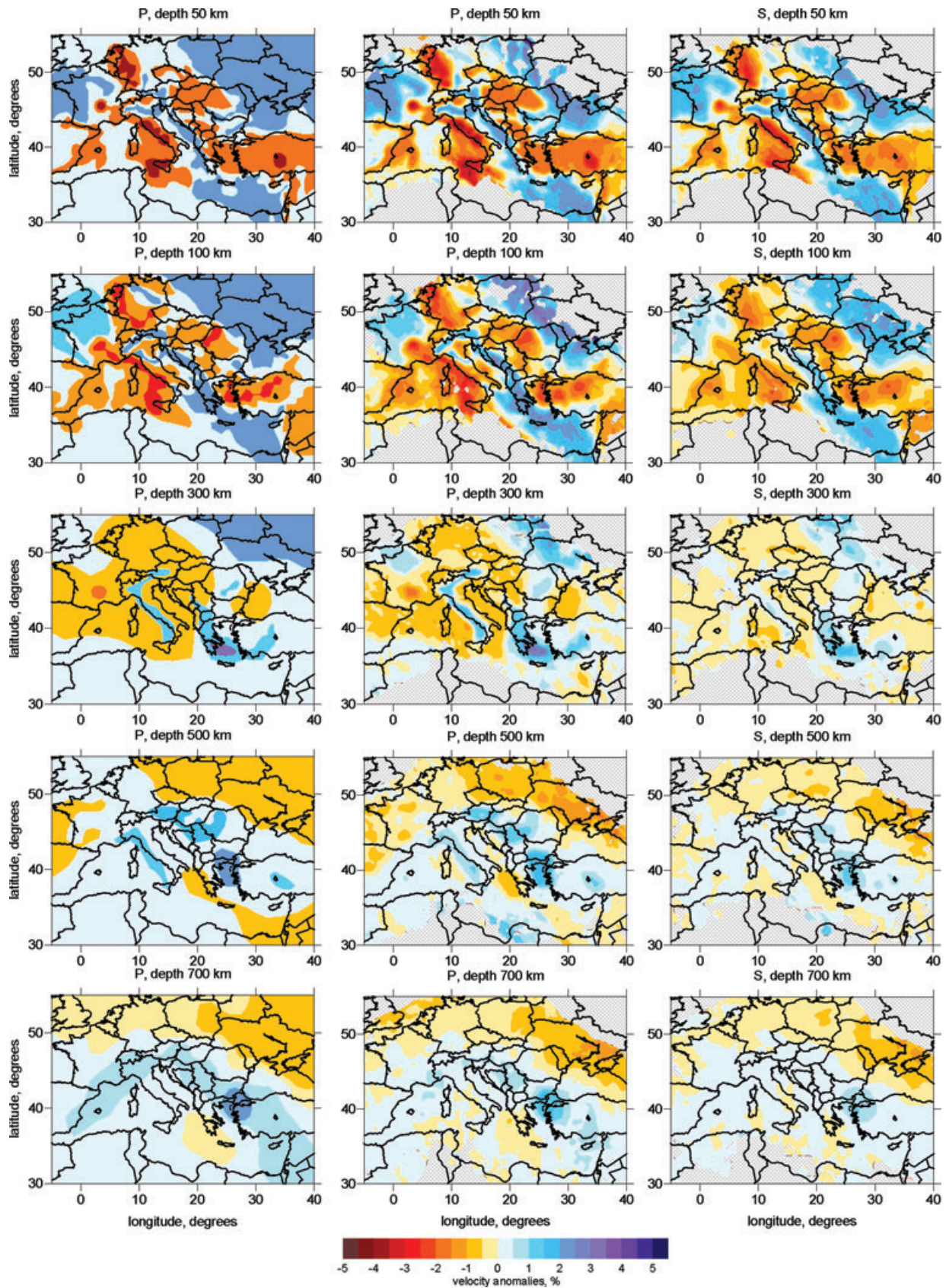
Figure 13. Synthetic reconstruction of a model with realistic distributions of anomalies. Configurations of synthetic model in some depth slices are shown in the left columns. The reconstructed *P* and *S* models are shown in the middle and right-hand columns. The shape and amplitudes of the synthetic anomalies were defined to obtain reconstruction results most similar to real data inversion (Figs 5 and 6). We added a random noise having an amplitude of 0.5 and 1 s for *P* and *S* data, respectively, to obtain the same values of variance reduction as in case of real data inversion.

anomalies in the same depth range beneath a part of the Eastern Carpathians only. At greater depths the *S* and *P* models are remarkably different: high velocities dominate in the first model, while low ones in the second, possibly on account of the lower resolution of the *S* model in this area.

In the eastern Carpathians, below the Vrancea zone, fast velocities (2 per cent) are found between 100 and 200 km in both *P* and *S* model. Between 200 and 300 km the fast anomaly is persistent only in the *P* model, becoming stronger than at shallow depths (cross-section 6). This high-velocity body has been a subject of many seismic studies (e.g. Oncescu *et al.* 1984; Oncescu *et al.* 1999; Cloetingh *et al.* 2004), being the locus of intermediate depth earthquakes (mostly range from 70 to 180 km). Previous authors have given different interpretations of the origin, nature and extension of this body. According to one hypothesis this body is a detached remnant of the oceanic lithosphere slab (e.g. Wenzel *et al.* 1998). According to the second one, it represents a small fragment of the oceanic lithosphere still attached to the continental lithosphere (Fan *et al.* 1998). The recent high-resolution teleseismic study of Martin *et al.* (2006) has imaged the high-velocity body beneath Vrancea in the depth range from 70 to 350 km with a change of orientation from NE–SW to N–S at ∼200 km. They interpret the deep aseismic part of the body below 200 km as decoupled from the overlying lithosphere.

4.5 Dinaric arc and Aegean subduction zone

At a depth of about 50 km both the *P* and *S* model show the whole Aegean Sea underlined by a wide pronounced negative anomaly (−2 per cent), which decreases in size and attenuates (−1 per cent) at greater depths down to ∼250 km (cross-sections 7 and 11). Furthermore, a strong positive anomaly (up to 3 per cent) is observed in the upper mantle from the top to ∼250 km beneath the Hellenic Arc, which joins with the fast anomaly (2 per cent) below the Dinarides. Both *P*- and *S*-model point to a thick lithosphere (∼200 km) beneath the Dinaric arc (cross-sections 1, 4 and 5), which is interpreted as a signature of the subducted Adriatic plate (e.g. Spakman 1993). However, a clear image of the descending slab east and west of the Adriatic micro-plate is only visible in cross-section 5 of the *P* model. In particular, we observe that the slab subducting beneath the Dinarides reaches a shallower depth (∼200 km) than below the Apennines. At greater depths (>300 km), the high velocity anomaly beneath the Dinaric Arc attenuates, while the anomaly below the Hellenides shifts northeastward, underlying the shallow low velocity structure under the Aegean Sea, and extending down to the bottom of the model. A similar structure has been already revealed by previous studies that interpret the fast velocity structure as the African lithosphere subducted beneath the Aegean plate. However, Spakman *et al.* (1988) observe a discontinuity in the high-velocity zone at a depth of 100–250 km interpreted as a detachment of the lower part of the slab (Wortel & Spakman 2000). In contrast, regional tomography and receiver functions studies do not show any significant gap in the positive anomaly at these depths (e.g. Papazachos *et al.* 1995; Papazachos & Nolet 1997; Sodoudi *et al.* 2006). At greater depths the continuous slab is visible even in the lower mantle down to 1200 km (Bijwaard *et al.* 1998; Karason & Van Der Hilst 2000). Both *P* and *S* models of the present study image a continuous high-velocity body (with a lateral velocity contrast >3.5 per cent) almost horizontal in the first 50–100 km and steeply dipping (∼45°) at greater depths down to the bottom of the model (cross-sections 6 and 7). Furthermore, we observe attenuation of the fast anomaly at the top of the

TZ, possibly due to a mineralogical phase change occurring at this depth in cross-sections 6, 7 and 11. Cross-section 11 also reveals a flattening of the subducted plate at the TZ. Previous studies (e.g. Faccenna *et al.* 2003; Widiyantoro *et al.* 2004) have demonstrated that the discontinuity at the bottom of the TZ produces a severe distortion of the flow trajectory, trapping slabs into the upper mantle (e.g. beneath the Calabrian arc, cross-section 9) or producing their deflection, like in the present case. The mechanism controlling the different behaviour of the slab is still poorly understood, but it might depend on the amount of subducted material and on the way in which it cumulates at the TZ (e.g. Faccenna *et al.* 2003). Furthermore, we observe a gradual steeping of the slab from west to east (cross-sections 6, 7 and 11), leading to a more rapid sinking of the African plate beneath the eastern part, as previously observed in some global (e.g. Piromallo & Morelli 2003) and regional (e.g. Papazachos *et al.* 1995) tomograpy studies. Therefore, we can assume that the slab deflection, which is observed in our model only in the easternmost part, can be related to the higher subduction velocity, which resulted in a larger amount of cold material accumulated in the deepest mantle layers. In this area a very good consistency between the *P* and *S* model is found, on account of the high positive correlation existing between their anomalies. In particular, the *S*-model images the slab subducted in greater detail than previous models (e.g. Marone *et al.* 2004), detecting this feature only in the first 300 km, losing resolution in the deeper layers.

5 CONCLUSIONS

1. We present a new tomographic model for *P*- and *S*-velocity anomalies beneath Europe (30°N–55°N, 5°W–40°E), extending in depth up to 700 km and constrained by inversion of ISC data. Different to previous models for the entire region, all traveltimes were corrected for the crustal structure using the reference model EuCRUST-07. This provides a basis for a better discrimination between crustal and mantle heterogeneity.

2. The sensitivity tests for the *P* model show a relatively high-horizontal resolution for the most of the European region, while for the *S* model there areas lacking resolution (e.g. beneath France). In these areas the amount of the *S*-wave teleseismic rays is not sufficient to retrieve any relevant information. The vertical resolution of the *P* model is good for the entire upper mantle and partially acceptable at the transition zone.

3. We generally observe a good consistency between the *P* and the *S* model for most of the area in the upper 200 km. Nearly all features are clearly imaged in this depth range in both models, such as the thick lithosphere below the Alps and the Dinarides. For some structures we can trace corresponding anomalies even at greater depths, like the Adriatic and the African plate subducted beneath the Apennines and the Aegean Sea, respectively. In these areas a high-positive correlation between *P*- and *S*- anomalies are found. In particular the *S*-model images the slab subducted with higher details than previous models (e.g. Marone *et al.* 2004). A disagreement between the two models is instead observed close to the edges of the study area (e.g. in the Carpathians) and in some other parts at a depth greater than 200 km (e.g. in the Alps, where the subducted slab is imaged only in the *P* model), on account of the loss of resolution of the *S* model.

4. Although both models are in general agreement with previous global tomographic *P* and *S* studies for the entire region, they provide higher resolution, which allows imaging small-scale anomalies in greater details (e.g. the slow velocity body beneath the Massif Central). A comparison between the *P* and the *S* model, where they

have good correlation, has confirmed some previous results (e.g. the gap in the Adriatic Plate subducted below the central-southern Apennines) and allowed to discriminate between hypotheses on the nature of the observed anomaly.

ACKNOWLEDGMENTS

REFERENCES

Alinaghi, A., Koulakov, I. & Thybo, H., 2007. Seismic tomographic imaging of *P*- and *S*-waves velocity perturbations in the upper mantle beneath Iran. *Geophys. J. Int.,* **169**(3), 1089–1102, doi:10.1111/j.1365–246X.2007.03317.x.

Al-Lazki, A., Sandvol, E., Seber, D., Barazangi, M., Turkelli & Mohamad, R., 2004. *Pn* tomographic imaging of mantle lid velocity and anisotropy at the juction of the Arabia, Eurasia and African plates, *Geophys. J. Int.,* **158,** 1024–1040.

Amato, A. *et al*., 1998. Passive seismology and deep structure in Central Italy, *Pure appl. Geophys.*, **151,** 479–493.

Artemieva, I., Thybo, H. & Kaban, M.K., 2006. Deep Europe today: geophysical synthesis of the upper mantle structure and lithospheric processes over 3.5 Ga, in *European Lithosphere Dynamics,* Vol. 32, pp. 11–41, eds Gee, D. & Stephenson, R., Geological Society, London, Memoirs.

Bassin, C., Laske, G. & Masters, G., 2000. The Current limits of resolution for surface wave tomography in North America, *EOS Trans AGU,* **81,** F897.

Berry, M.J. & Knopoff, L., 1967. Structure of the upper mantle under the western Mediterranean Basin, *J. geophys. Res.,* **72**(14), 3613–3626.

Bijwaard, H. & Spakman, W., 2000. Non-linear global P-wave tomography by iterated linearized inversion, *Geophys. J. Int.,* **141,** 71–82.

Bijwaard, H., Spakman, W. & Engdahl, E.R., 1998. Closing the gap between regional and global travel time tomography, *J. geophys. Res.,* **103,** 30 055–30 078.

Blanco, M.J. & Spakman, W., 1993. The P-wave velocity structure of the mantle below the Iberian peninsula: evidence for subducted lithosphere below southern Spain, *Tectonophysics,* **221,** 13–34.

Calcagnile, G. & Panza, G.F., 1981. The main characteristics of the lithosphere-asthenosphere system in Italy and surrounding regions, *Pure appl. Geophys.,* **119,** 865–879.

Calcagnile, G. & Panza, G.F., 1990. Crustal and upper mantle structure of the Mediterranean area derived from surface-wave data, *Phys. Earth planet. Inter.,* **60,** 163–168.

Calcagnile, G., D'Ingeo, F., Farrugia, P. & Panza, G.F., 1982. The lithosphere in the central-eastern Mediterranean area, *Pure appl. Geophys.,* **120,** 389–406.

Calvert, A. *et al*., 2000. Geodynamic evolution of the lithosphere and upper mantle beneath the Alboran region of the western Mediterranean: Constraints from travel time tomography, *J. geophys. Res.,* **105,** 10 871–10 898.

Chiarabba, C., De Gori, P. & Speranza, F., 2008. The southern Tyrrhenian subduction zone: deep geometry, magmatism and Plio-Pleistocene evolution, *Earth planet. Sci. Lett.,* **268,** 408–423.

Cimini, G.B. & De Gori, P., 2001. Nonlinear P-wave tomography of subducted lithosphere beneath central-southern Apennines (Italy), *Geophys. Res. Lett.,* **28**(23), 4387–4390.

Cloetingh, S.A.P.L., Burov, E., Matenco, L., Toussaint, G., Bertotti, G., Andriessen, P.A.M., Wortel, M.J.R. & Spakman, W., 2004. Thermomechanical controls on the mode of continental collision in the SE Carpathians (Romania), *Earth planet. Sci. Lett.,* **218,** 57–76.

Curtis, A., Trampert, J., Snieder, R. & Dost, B., 1998. Eurasian fundamental mode surface wave phase velocities and their relationship with tectonic structures, *J. geophys. Res.,* **103,** 26 919–26 947.

de Jonge, M.R., Wortel, M.J.R. & Spakman, W., 1994. Regional scale tectonic evolution and the seismic velocity structure of the lithosphere and upper mantle: the Mediterranean region, *J. geophys. Res.,* **99**(B6), 12 091–12 108.

Ekström, G. & Dziewonski, A.M., 1998. The unique anisotropy of the Pacific upper mantle, *Nature,* **394,** 168–172.

Engdahl, E.R., Van Der Hilst, R. & Buland, R., 1998. Global teleseismic earthquake relocation with improved travel times and procedures for depth determination, *Bull. seism. Soc. Am.,* **88,** 722–743.

Faccenna, C., Jolivet, L., Piromallo, C. & Morelli, A., 2003. Subduction and the depth of convection in the Mediterranean mantle, *J. geophys. Res.,* **108**(B2), 2099, doi:10.1029/2001JB001690.

Fan, G., Wallace, T.C. & Zhao, D., 1998. Tomographic imaging of deep velocity structure beneath the eastern and southern Carpathians, Romania: implications for continental collision, *J. geophys. Res.,* **103,** 2705–2723.

Galushkin, Yu.I., Shreider, A.A., Bulychev, A.A. & Shreider, Al.A., 2006. Heat flow and thermal evolution of the lithosphere of the Black Sea Basin, *Oceanology,* **46**(2), 274–291.

Gobarenko, V.S., Nikolova, S.B. & Sokolova, S.J., 1990. The velocity structure of the western Mediterranean from inversion of P-wave traveltime, *Geophys. J. Int.,* **101,** 557–564.

Goes, S., Spakman, W. & Bijwaard, H., 1999. A lower mantle source for central European volcanism, *Science,* **286,** 1928–1931.

Goes, S., Govers, R. & Vacher, P., 2000. Shallow mantle temperatures under Europe from *P* and *S* wave tomography, *J. geophys. Res.,* **105**(B5), 11 153–11 169.

Goek, R., Pasyanos, M.E. & Zor, E., 2007. Lithospheric structure of the continent–continent collision zone: eastern Turkey, *Geophys. J. Int.,* **169,** 1079–1088.

Granet, M. & Trampert, J., 1989. Large-scale P velocity structures in the Euro-Mediterranean area, *Geophys. J. Int.,* **99,** 583–594.

Gutscher, M.A., Malod, J., Rehault, J.P., Contrucci, I., Klingelhoefer, F., Mendes-Victor, L. & Spakman, W., 2002. Evidence for active subduction beneath Gibraltar, *Geology,* **30**(12), 1071–1074.

Hatzfeld, D. & the Working Group for Deep Seismic Sounding, 1978. Crustal Seismic profiles in the Alboran Sea Preliminary results, *Pure appl. Geophys,* **116,** 167–180.

Hearn, T.M., 1999. Uppermost mantle velocities and anisotropy beneath Europe, *J. geophys. Res.,* **104**(B7), 15 123–15 140.

Hovland, J., Gubbins, D. & Husebye, E.S., 1981. Upper mantle heterogeneities beneath Central Europe, *Geophys. J. R. astr. Soc.,* **66,** 261–284.

Hurtig, E., Cermak, V., Haenel, R. & Zui, V. (eds), 1992. *Geothermal Atlas of Europe, International Association for Seismology and Physics of the Earth's Interior,* 156 pp., Hermann Haack Verlagsgesellschaft mbH-Geographisch-Kartographische Anstalt Gotha.

International Seismological Centre, 2001. *Bulletin Disks 1–9 [CD-ROM],* Internatl. Seis. Cent., Thatcham, UK.

Jeffreys, H. & Bullen, K.E., 1940. *Seismological Tables,* British Association for the Advancement of Science, London.

Kaban, M.K., 2001. A Gravity Model of the North Eurasia Crust and Upper Mantle: 1. Mantle and Isostatic Residual Gravity Anomalies, *Russ. J. Earth Sci.* (maintained and distributed by AGU, http://www.agu.org/wps/rjes/), **3**(2), 143–163.

Kaban, M.K., Tesauro, M. & Cloetingh, S.A.P.L., 2009. A new gravity model of the crust and upper mantle of Europe, *Earth planet. Sci. Lett.,* submitted.

Karason, H. & Van Der Hilst, R.D., 2000. Constraints on mantle convection from seismic tomography, in *The History and Dynamics of Global Plate Motions,* Am. geophys. Union geophys. Monogr., Vol. 121, pp. 277–289, eds Richards, M., Gordon, R.G. & van der Hilst, R.D., American Geophysical Union.

Kennett, B.L.N., Engdahl, E.R. & Buland, R., 1995. Constraints on seismic velocities in the Earth from traveltimes, *Geophys. J. Int.,* **122,** 108–124.

Keyser, M., Ritter, J.R.R. & Jordan, M., 2002. 3D shear-wave velocity structure of the Eifel plume, Germany. *Earth planet. Sci. Lett.,* **203,** 59–82.

Koulakov, I., 2009. LOTOS code for local earthquake tomographic inversion: benchmarks for testing tomographic algorithms, *Bull. seism. Soc. Am.,* **99**(1), 194–214, doi:10.1785/0120080013.

Koulakov, I. & Sobolev, S.V., 2006. A Tomographic Image of Indian Lithosphere Break-off beneath the Pamir Hindukush Region, *Geophys. J. Int.,* **164,** 425–440.

Koulakov, I., Tychkov, S., Bushenkova, N. & Vasilevskiy, A., 2002. Structure and dynamics ovf the upper mantle beneath the Alpine-Himalayan orogenic belt, from teleseismic tomography, *Tectonophysics,* **358,** 77–96.

Koulakov, I., Sobolev, S.V., Weber, M., Oreshin, S., Wylegalla, K. & Hofstetter, R., 2006. Teleseismic tomography reveals no signature of the Dead Sea Transform in the upper mantle structure, *Earth. planet. Sci. Lett.,* **252**(1–2), 189–200.

Koulakov, I. *et al*., 2007. *P* and *S* velocity structure of the crust and the upper mantle beneath central Java from local tomography inversion, *J. geophys. Res.,* **112,** B08310, doi:10.1029/2006JB004712.

Koulakov, I.Yu., 1998. 3D tomographic structure of the upper mantle beneath the central part of Eurasian continent, *Geophys. J. Int.,* **133**(2), 467–489.

Koulakov, I.Yu., 2008. Mantle structure beneath Southern Siberia and Mongolia from regional seismic tomography, *Russ. Geol. Geophys,* **49**(3), 244–257.

Lenkey, L., 1999. Geothermics of the Pannonian basin and its bearing on the tectonics of Basin evolution, *PhD thesis*. Vrije Universiteit, Amsterdam, 215 pp.

Lippitsch, R., Kissling, E. & Ansorge, J., 2003. Upper mantle structure beneath the Alpine orogen from high-resolution teleseismic tomography, *J. geophys. Res.,* **108**(B8), 2376, doi:10.1029/2002JB002016.

Lucente, F.P. & Speranza, F., 2001. Belt bending driven by lateral bending of subducting lithosphere slab: geophysical evidences from the northern Apennines (Italy), *Tectonophysics,* **337,** 53–64.

Marillier, F. & Mueller, St., 1985. The western Mediterranean region as an upper-mantle transition zone between two lithospheric plates, *Tectonophysics,* **118,** 113–130.

Marone, F., Van Der Lee, S. & Giardini, D., 2004. Three-dimensional upper-mantle S-velocity model for the Eurasia-Africa plate boundary region, *Geophys. J. Int.,* **158,** 1–109.

Marquering, H. & Snieder, R., 1996. Shear-wave velocity structure beneath Europe, the northeastern Atlantic and western Asia from waveform inversions including surface-wave mode coupling, *Geophys. J. Int.,* **127,** 283–304.

Martin, M., Ritter, J.R.R. & the CALIXTO working group, 2005. High-resolution teleseismic body-wave tomography beneath SE Romania - I. Implications for threedimensional versus one-dimensional crustal correction strategies with a new crustal velocity model, *Geophys. J. Int.,* **162,** 448–460.

Martin, M., Ritter, J.R.R. & the CALIXTO working group, 2006. High-resolution teleseismic body wave tomography beneath SE-Romania–II. Imaging of a slab detachment scenario, *Geophys. J. Int.,* **164,** 579–595.

Martinez, M.D., Lana, X., Canas, J.A., Badal, J. & Pujades, L., 2000. Shear-wave velocity tomography of the lithosphere–asthenosphere system beneath the Mediterranean area, *Phys. Earth planet. Inter.,* **122,** 33–54.

Mele, G., Rovelli, A., Seber, D., Hearn, T.M. & Barazangi, M., 1998. Compressional velocity structure and anisotropy in the uppermost mantle beneath Italy and surrounding regions, *J. geophys. Res.,* **103,** 12 529–12 543.

Nolet, G., 1981. Linearized inversion of (teleseismic) data, in *The Solution of the Inverse Problem in Geophysical Interpretation,* pp. 9–37, ed. Cassinis, R., Plenum Press, New York.

Nolet, G., 1987. Seismic wave proportion and seismic tomography, in *Seismic Tomography, With Application, in Global Seismology and Exploration Geophysics,* pp. 1–27, ed. Nolet, G., Reidel, Dordrecht.

Nolet, G., 1990. Partitioned waveform inversion and two-dimensional structure under the Network of Autonomously recording Sesmograph, *J. geophys. Res.,* **95,** 8499–8512.

Olaiz, A.J., Muñoz-Martín, A., De Vicente, G., Vegas, R. & Cloetingh, S., 2009. European continuous active tectonic strain-stress Map, *Tectonophysics,* in press.

Oncescu, M.C., Burlacu, V., Angel, M. & Smalbergher, V., 1984. Three-dimensional P-wave velocity image under the Carpathian arc, *Tectonophysics,* **106,** 305–319.

Oncescu, M.C., Marza, V.I., Rizescu, M. & Popa, M., 1999. The Romanian earthquake catalogue between 984–1997, in *Vrancea Earthquakes: tectonics,Hazard and Risk Mitigation,* pp. 27–42, eds Wenzel, F., Lungu, D. & Novak, O., Kluwer Academic Publisher, Dordrecht.

Paige, C.C. & Saunders, M.A., 1982. LSQR: An algorithm for sparse linear equations and sparse least squares, *ACM trans. Math. Soft.,* **8**(1), 43–71.

Panza, G.F., Mueller, St. & Calcagnile, G., 1980. The gross features of the lithosphere-asthenosphere system in Europe from seismic surface waves and body waves, *Pure appl. Geophys.,* **118,** 1209–1213.

Papazachos, C. & Nolet, G., 1997. P and S deep velocity structure of Hellenic area obtained by robust nonlinear inversion of travel times, *J. geophys. Res.,* **102,** 8349–8367.

Papazachos, C.B., Hatzidimitriou, P.M., Panagiotopoulos, D.G. & Tsokas, G., 1995. Tomography of the crust and upper mantle in southeast Europe, *J. geophys. Res.,* **100,** 12 405–12 442.

Pasyanos, M., 2005. A variable resolution surface wave dispersion study of Eurasia, North Africa, and surrounding regions, *J. geophys. Res.,* **110,** B12301, doi:10.1029/2005JB003749.

Pasyanos, M.E., Walter, W.R. & Hazler, S.E, 2001. A Surface Wave Dispersion Study of the Middle East and North Africa for Monitoring the Comprehensive Nuclear-Test-Ban Treaty, *Pure appl. Geophys.,* **158**(8), 1445–1474.

Piromallo, C. & Faccenna, C., 2004. How deep can we find the traces of Alpine subduction?, *Geophys. Res. Lett.,* **31,** L06605, doi:10.1029/2003GL019288.

Piromallo, C. & Morelli, A., 2003. P wave tomography of the mantle under the Alpine-Mediterranean area, *J. geophys. Res.,* **108**(B2), doi:10.1029/2002JB001757.

Plomerová, J., Achauer, U., Babuška, V., Vecsey, L. & BOHEMA working group, 2007. Upper mantle beneath the Eger Rift (Central Europe): plume or asthenosphere upwelling?, *Geophys. J. Int.,* **169,** 675–682.

Polyak, B.G. *et al*., 1996. Heat flow in the Alboran Sea, western Mediterranean, *Tectonophysics,* **263,** 191–218.

Ritter, J.R.R., 2007. The seismic signature of the Eifel plume, in *Mantle Plumes—A Multidisciplinary Approach,* pp. 159–184, eds Ritter, J.R.R. & Christensen, U.R., SpringerVerlag, Heidelberg.

Romanowicz, B.A., 1980. A study of large-scale lateral variations of *P*-velocity in the upper mantle beneath western Europe, *Geophys. J. R. astr. Soc.,* **63,** 217–232.

Sandoval, S., Kissling, E., Ansorge, J. & the SVEKALAPKO Seismic TomographyWorking Group, 2003. High-resolution body wave tomography beneath the SVEKALAPKO array: I. A priori three-dimensional crustal model and associated traveltime effects on teleseismic wave fronts, *Geophys.J. Int.,* **153,** 75–87.

Schmid, C., Van Der Lee, S. & Giardini, D., 2006. Correlated shear and bulk moduli to 1400 km beneath the Mediterranean region, *Phys. Earth planet. Inter.,* **159,** 213–224.

Snieder, R., 1988. Large scale waveform inversions of surface waves for lateral heterogeneity, 2, Application to surface waves in Europe and the Mediterranean, *J. geophys. Res.,* **93,** 12,067–12,080.

Sodoudi, F. *et al*., 2006. Lithospheric structure of the Aegean obtained from P and S receiver functions, *J. geophys. Res,* **111**(B12), doi:10.1029/2005JB003932.

Spakman, W., 1991. Delay-time tomography of the upper mantle below Europe, the Mediterranean, and Asia Minor, *Geophys. J. Int.,* **107,** 309–332.

Spakman, W., 1993. Tomographic images of the upper mantle below central Europe and the Mediterranean, *Terra Nova,* **2,** 542–553.

Spakman, W., Wortel, M.J.R. & Vlaar, N.J., 1988. The Hellenic subduction zone: A tomographic image and its geodynamic implications, *Geophys. Res. Lett.,* **15,** 60–63.

Spakman, W., Van Der Lee, S. & Van Der Hilst, R., 1993. Traveltime tomography of the European-Mediterranean mantle down to 1400 km, *Phys. Earth planet. Inter.,* **79,** 3–74.

Środa, P. *et al.,* CELEBRATION 2000 Working Group, 2006. Crustal and upper mantle structure of the Western Carpathians from CELEBRATION 2000 profiles CEL01 and CEL04: seismic models and geological implications, *Geophys. J. Int.,* **167,** 737–760.

Tesauro, M., Kaban, M.K., Cloetingh, S.A.P.L., Hardebol, N.J. & Beekman, F., 2007. 3D strength and gravity anomalies of the European lithosphere, *Earth planet. Sci. Lett.,* **263,** 56–73.

Tesauro, M., Kaban, M.K. & Cloetingh, S.A.P.L., 2008. EuCRUST-07: a new reference model for the European crust, *Geophys. Res. Lett.,* **35,** L05313, doi:10.1029/2007GL032244.

Van Der Sluis, A. & van der Vorst, H.A., 1987. Numerical solution of large, sparse linear algebraic systems arising from tomographic problems, in *Seismic Tomography,* pp. 49–83, ed. Nolet, G., Reidel, Dordrecht.

Vignaroli, G., Faccenna, C., Jolivet, L., Piromallo, C. & Rossetti, F., 2008. Subduction polarity reversal at the junction between the Western Alps and the Northern Apennines, Italy, *Tectonophysics,* **450,** 34–50, doi:10.1016/j.tecto.2007.12.012.

Waldhauser, F., Lippitsch, R., Kissling, E. & Ansorge, J., 2002. High-resolution teleseismic tomography of upper mantle structure using an a priori 3D crustal model, *Geophys. J. Int.,* **150,** 141–403.

Wéber, Z., 2002. Imaging Pn velocities beneath the Pannonian basin, *Phys. Earth planet Inter.,* **129**(2002) 283–300.

Wenzel, F., Achauer, U., Enescu, D., Kissling, E., Russo, R., Mocanu, V. & Musacchio, G., 1998. Detailed look at final stage of break-off is target of study in Romania, *Eos Trans. AGU,* **48,** 589–594.

Widiyantoro, S., Van Der Hilst, R.D. & Wenzel, F., 2004. Deformation of the Aegean slab in the upper mantle transition zone, *Int. J. Tomogr. Stat.,* **D04,** 1–14.

Wortel, M.J.R. & Spakman, W., 1992. Structure and dynamics of subducted lithosphere in the Mediterranean region, *Res. Neth. Acad. Sci.,* **95,** 325–347.

Wortel, M.J.R. & Spakman, W., 2000. Subduction and slab detachment in the Mediterranean-Carpathian Region, *Science,* **290,** 1910–1917.

Ziegler, P.A., 1992. North Sea Rift System. in *Geodynamics of Rifting,* Vol. I, pp. 55–75, ed. Ziegler, P.A., Case History Studies–Rifts, Europe and Asia, *Tectonophysics,* **208**.

Ziegler, P.A. & Dèzes, P., 2006. Crustal evolution of Western and Central Europe, in *European Lithophere Dyanamics*, Vol. 32, pp. 43–56, eds Gee, D. & Stephenson, R., Geological Society, London.

Zielhuis, A. & Nolet, G., 1994. Shear-wave velocity variations in the upper mantle beneath central Europe, *Geophys. J. Int.,* **117,** 695–715.

Zito, G., Mongelli, F., de Lorenzo, S. & Doglioni, C., 2003. Heat flow and geodynamics in the Tyrrhenian Sea, *Terra Nova,* **15,** 425–432.